FOUR-ARM GRATING COUPLERS FOR WAVEFRONT SENSING APPLICATIONS

FOUR-ARM GRATING COUPLERS FOR WAVEFRONT SENSING APPLICATIONS

By ALEXANDER PARENT, B.Eng

A Thesis Submitted to the School of Graduate Studies in Partial Fulfillment of the Requirements for the Degree of Master of Applied Science

McMaster University

Master of Applied Science (2023)

Hamilton, Ontario (Department of Engineering Physics)

TITLE: Four-Arm Grating Couplers for Wavefront Sensing Applications

AUTHOR: Alexander Parent (McMaster University)

SUPERVISOR: Dr. Rafael Kleiman

NUMBER OF PAGES: xiii, 85

Abstract

Atmospheric turbulence in free space optical satellite downlinks negatively impacts link availability and bit error rate. These effects can be mitigated using a compensation system capable of measuring the incoming wavefront distortion and applying a suitable correction to the received signal. The traditional solution based on adaptive optics and the Shack-Hartmann wavefront sensor has limitations in bandwidth, system complexity, size, weight, and power consumption. Signal correction can also be accomplished using a novel single-chip silicon photonic solution. This work introduces a four-arm grating coupler structure acting as a wavefront sensing element that emulates the performance of the Shack-Hartmann wavefront sensor by giving local tip and tilt estimation. FDTD simulations and measurements have confirmed the presence of a monotonic relationship between incident angle, polarization, and coupler output which can be converted to phase estimation through a reconstruction algorithm. An array of four-arm couplers on a silicon photonic chip provides enough sampling to fully reconstruct the wavefront, providing benefits over traditional solutions such as higher bandwidth, reduced size and weight, and reduced cost. Scaling up the results of this work to a full device could provide a solution for free space optical satellite to ground links in remote and rural communities across Canada and around the world.

Acknowledgements

I would like to thank my supervisor, Dr. Kleiman, for his support and guidance throughout this project. I initially decided to pursue a graduate degree to advance my technical skills and work on interesting problems with interesting people, and that describes the opportunity that he has provided. I would also like to thank my main collaborator in all things silicon photonic, Aydin Amini, for our interesting chats and sharing of skills and knowledge. CMC Microsystems and SiEPIC also deserve recognition for providing workshops and facilitating accessible silicon photonic prototyping for Canadian graduate students. This work would not have been possible without them.

I would also like to thank my mom, dad, and sister for their support through my master's degree and entire life; they have always supported me and encouraged me to find a passion and pursue it. A love of science and discovery was instilled in me at an early age, and I thank them for that.

Finally, thank you to Patricia for being the best, most encouraging, and most understanding person I have ever met. You make me excited for the future.

Table of Contents

List of Figures

List of Tables

List of abbreviations and symbols

5G Fifth Generation

6G Sixth Generation

ANT Applied Nanotools Inc.

AO Adaptive Optics

AV Autonomous Vehicle

BER Bit Error Rate

BOX Buried Oxide

DBR Distributed Bragg Reflector

DUT Device Under Test

DWDM Dense Wavelength Division Multiplexing

EBL Electron Beam Lithography

FDTD Finite Difference Time Domain

FSO Free Space Optics

Gbps Gigabit per second

GEO Geostationary Earth Orbit

HWP Half Wave Plate

LEO Low Earth Orbit

MEMS Micro Electromechanical Systems

mmW Millimetre Wave

NIR Near Infrared

OPA Optical Phased Array

PBS Polarization Beam Splitter

PD Photodiode

QAM Quadrature Amplitude Modulation

RF Radio Frequency

RIE Reactive Ion Etching

SEM Scanning Electron Microscopy

SHWFS Shack-Hartmann Wavefront Sensor

SiN Silicon Nitride

SOI Silicon on Insulator

SWG Subwavelength Grating

TE Transverse Electric

TO Topology Optimization

TOPS Thermo-optic Phase Shifter

TOX Top Oxide

Declaration of Academic Achievement

I, Alexander Parent, declare that this thesis titled “Four-Arm Grating Couplers for Wavefront Sensing Applications” and the work presented in it are my own. All references to other works are clearly cited.

Contributions by others are always indicated where relevant. Notably:

1. On page 48, preliminary designs for the 572 nm nanohole four-arm grating couplers were done by Ruslan Khabibrakhmanov
2. On page 61, measurement setup automated scanning code was contributed to by Archie Dubey
3. On page 63, simulations used to verify tip/tilt performance of the 572 nm four-arm grating couplers were done by Aydin Amini

Introduction

Humanity's ability to communicate is inherently tied to technological and societal development. Advances ranging from the printing press to the Internet have fundamentally changed the way we share ideas and collaborate as a species. In the modern era, fiber optic technology is enabling high data rate communications worldwide using optical signals, forming the backbone of the internet. For many remote and rural communities however, deploying fiber infrastructure is not always feasible for geographical or financial reasons. Free space optical (FSO) satellite networks can provide secure and reliable network connectivity around the globe.

Free Space Optical Telecommunication Links

Free space optical links use infrared and visible carrier signals to transfer information between a transmitter and receiver over an unguided channel. Optical signals provide a few key advantages over traditional radio frequency (RF) links, including large bandwidth, low power consumption, low beam divergence, high data rate and increased security [1]. Optical networks comprised of geostationary Earth orbit (GEO) satellites, low earth orbit (LEO) satellites, ground stations, and aircraft can also provide connectivity to remote and rural communities where installation of traditional infrastructure like fiber is impossible or infeasible. An example of this type of network is shown schematically in Figure 1.

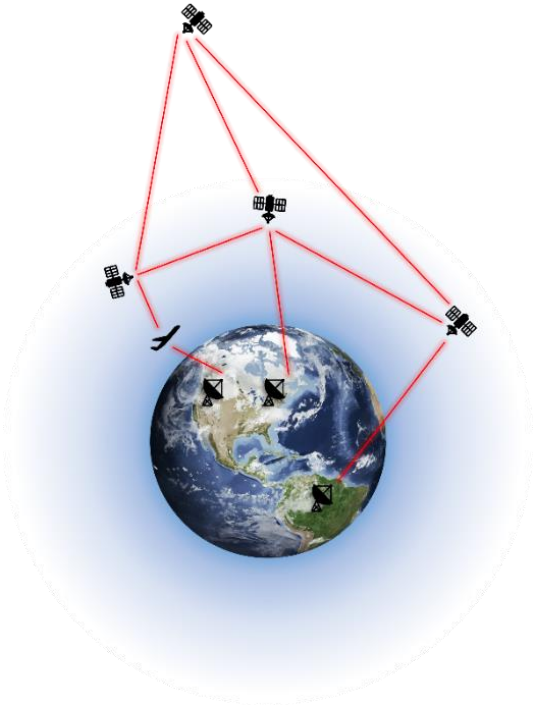

Figure 1: Visualization of an FSO network including satellite to ground links.

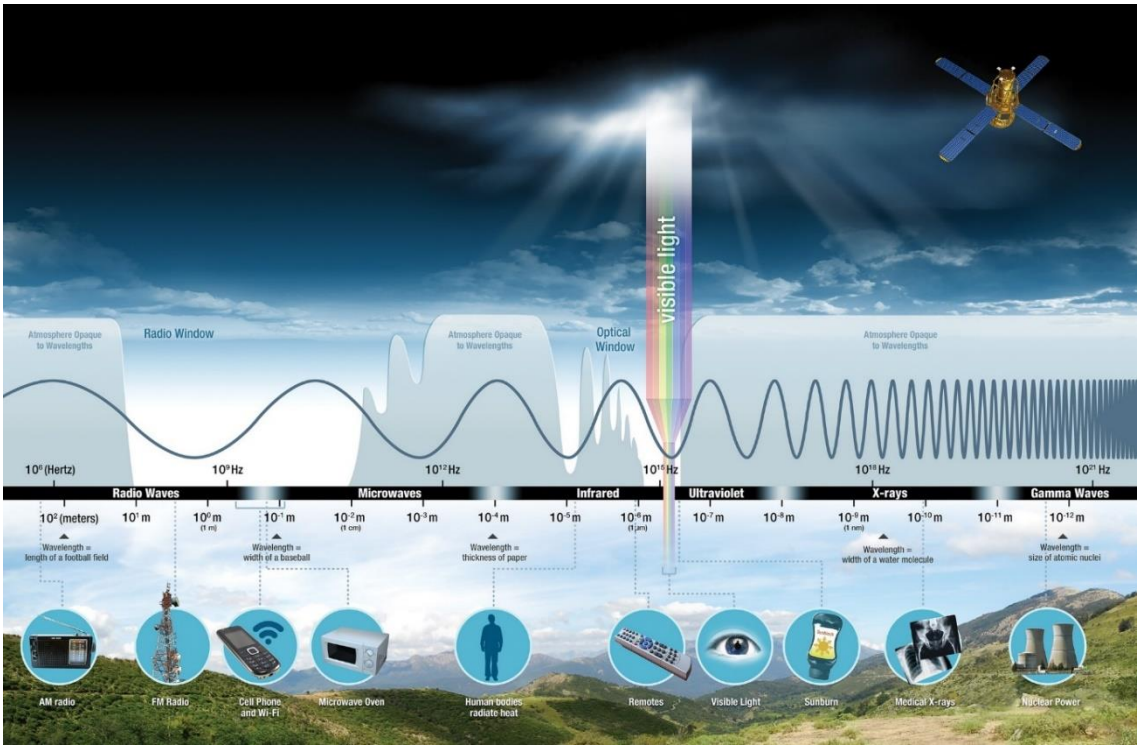

Figure 2: Common uses of various bands in the electromagnetic spectrum [2].

Satellite-to-ground communication is traditionally done using the C, K_u, and K_a bands ranging in frequency from 4-40 GHz. A typical C-band link has a 500 MHz bandwidth divided into 12 channels [3]. Modern 5G systems utilize millimeter wave (mmW) band transmission between 30-300 GHz to provide gigabit per second (Gbps) data rates. It has been proposed that sixth generation (6G) technology use the upper mmW and THz regimes to provide even higher bandwidth, though atmospheric absorption from oxygen at 60 GHz and water at 300 GHz impacts link budgets by reducing transmitted power [4]. Utilization of these new bands could allow wireless links to achieve much higher data rates [5].

FSO links commonly operate in the near infrared (NIR) at 1550 nm (200 THz), which is the same wavelength used in fiber optics telecom. The much shorter wavelength massively increases bandwidth allowing much higher data rates. In fiber optics, dense wavelength division multiplexing (DWDM) supports many closely spaced channels on a single fiber resulting in data rates up to 800 Gbps. The record data rate transmitted over the fiber optic C-band as of 2022 is 1.53 Pbps, achieved using 184 wavelength channels and 16-quadrature-amplitude modulation (QAM) [6]. This result demonstrates the potential of optical communication signals.

Many bidirectional intersatellite FSO links have been demonstrated as these do not have to contend with atmospheric turbulence when there is a direct line of sight between transmitter and receiver through space. One such link has been demonstrated by Seel et al. in which transmitted bit errors only occurred when the optical path grazed the atmosphere. This work also demonstrated coherent laser communication to ground

stations for the first time, and showed a stronger effect of turbulence at lower elevations and larger incident angles [7]. NASA's Laser Communications Relay Demonstration (LCRD) launched in 2021 enables 1.2 Gbps optical communication between two ground station locations in California and Hawaii [8]. The system is also equipped with a high-bandwidth RF link to ensure availability even in poor seeing conditions, which the authors note may be the preferred architecture in future GEO optical satellite networks [9]. The optical link supports very high data rate but with occasional service outages while the RF link provides reliable but much lower data rate service. The current record-holding satellite to ground optical link was achieved in December 2022 by the TeraByte InfraRed Delivery (TBIRD) system at 200 Gbps from a LEO satellite [10]. The system can transmit over 1 TB of data error-free over a single five-minute pass, depending on atmospheric conditions. The ground station consists of a 1 m telescope and adaptive optics system at JPL's Optical Communications Telescope Laboratory (OCTL) in California [11].

Atmospheric Turbulence

A major impediment to FSO communication is the presence of atmospheric turbulence along the path of the beam causing both phase distortions and signal fading. These distortions arise from fluctuations in the refractive index of air due to temperature and pressure gradients which are inherently stochastic and time-varying phenomena [12]. The magnitude of the distortion due to small scale turbulence is described by the refractive index structure coefficient C_n^2 which is a complex and nonlinear function of temperature, pressure and humidity [13]. This varies with altitude, viewing angle, season, and time of

day at a given geographical location. The maximum achievable imaging resolution is defined by the Fried parameter, which is the integral of C_n^2 over the optical path [14]. This Fried parameter describes the diameter of a circle over which the rms wavefront error is one radian. Atmospheric turbulence has a negative effect on bit error rate and link reliability as the phase distortions can be larger than 2π and signal fading can be in the tens of decibels [15]. Physical or computational distortion compensation is therefore required to improve satellite to ground FSO feasibility.

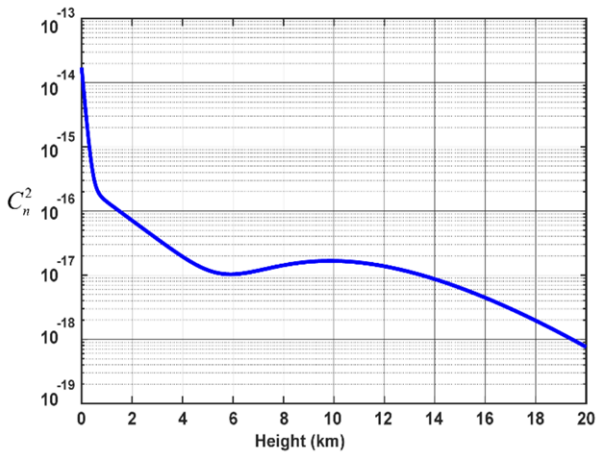

Figure 3: Typical relationship between C_n^2 and altitude [16].

The magnitude of atmospheric distortions depends on altitude and climate, meaning some locations are more ideal for FSO ground stations than others. Weather including cloud cover and precipitation also degrades optical links through attenuation and scattering, meaning different locations around the world present unique challenges [17]. The effects of weather-based link outages can be mitigated using site-diversity techniques with multiple ground stations installed many kilometres from each other and connected via a

terrestrial backbone [18]. This increases the likelihood that at least one ground station can support a functional link at any given time.

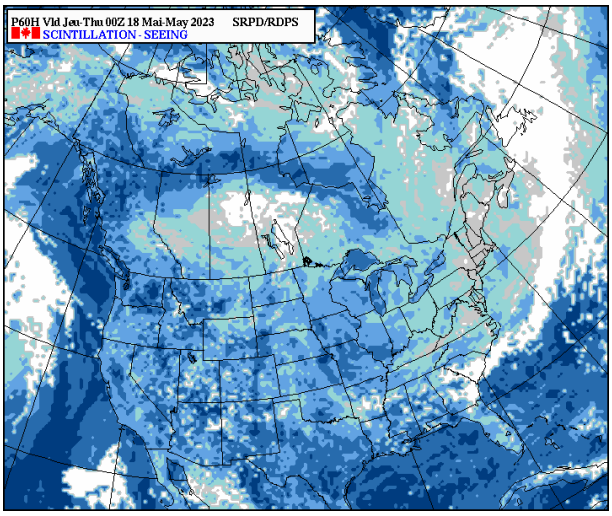

Figure 4: Seeing parameter distribution across North America [19].

The speed at which the distortions due to turbulence change is known as the Greenwood frequency and is an important parameter in systems that deal with mitigating turbulent effects. These systems must respond with a bandwidth of at least the Greenwood frequency to keep up with the changing received wavefront characteristic and obtain good performance [20]. In a satellite downlink application this value depends on C_n^2, optical path, wind speed and satellite speed if the deployment is LEO. Typical values of Greenwood frequency for astronomical applications, or those in favourable seeing conditions without a satellite movement contribution, can reach kilohertz. The previously mentioned LCRD achieved an operational bandwidth of 20 kHz, which the authors state is high enough for LEO operation [21]. It should be noted that favourable ground station

locations were used, and control frequencies may need to be much higher for deployment in urban and remote regions with less favourable seeing conditions.

Mitigation Techniques

There are many different approaches to mitigating atmospheric turbulence in both the physical and computational domains. One approach is adaptive optics (AO), commonly used in astronomy applications to improve image quality. The AO system consists of three parts, a deformable mirror, wavefront sensor, and control system which provide wavefront correction, error estimation, and feedback respectively as seen in Figure 5 [12]. A small portion of the incoming signal is split off and sent to the sensor which measures the distortion across the wavefront. A complete picture of the distortion can then be obtained using a reconstruction algorithm, which is fed to the deformable mirror. The corrected output approximates a Gaussian beam which is coupled into a fiber for further processing.

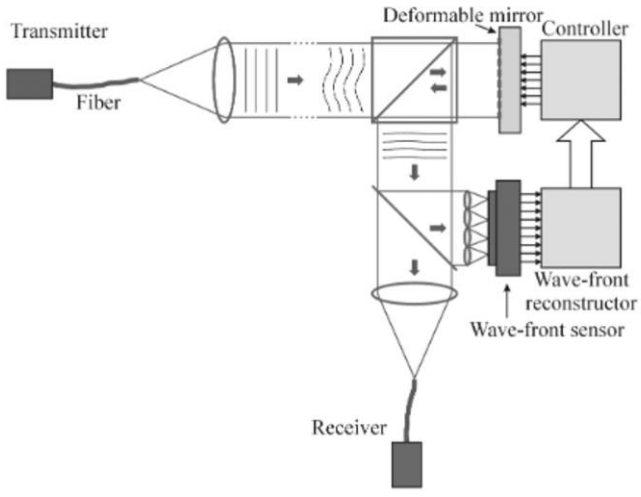

Figure 5: Typical layout of an AO system for communication [22].

Adaptive optics is a mature technology and has been used successfully in FSO links. However, deformable mirrors are slow and contain a limited number of actuating elements limiting the type of compensation they can provide. The low bandwidth of an AO system means higher order aberrations cannot be corrected. Either a multi-stage AO system or separate approach is desirable to improve bit error rate (BER) and link availability [23]. Advances in micro-electromechanical systems (MEMS) technology may also improve the outlook for AO systems in FSO [22].

Wavefront sensors are devices that measure aberrations within an optical wavefront and provide the information required for correction with a deformable mirror or similar device. There are several distinct types of wavefront sensors. For adaptive optics, the common solution is the Shack-Hartmann wavefront sensor (SHWFS). It consists of an array of independent lenslets each focused onto an arrayed detector placed at the lenslet focal length. In the case of an undistorted wavefront each lenslet produces a focal spot directly on its optical axis. Distortion in a wavefront laterally displaces the focal spot by an amount proportional to the gradient of the wavefront across the lenslet. This transforms the phase error of the wavefront to a set of locally measurable tilts, from which the wavefront can be reconstructed using a reconstruction algorithm [24].

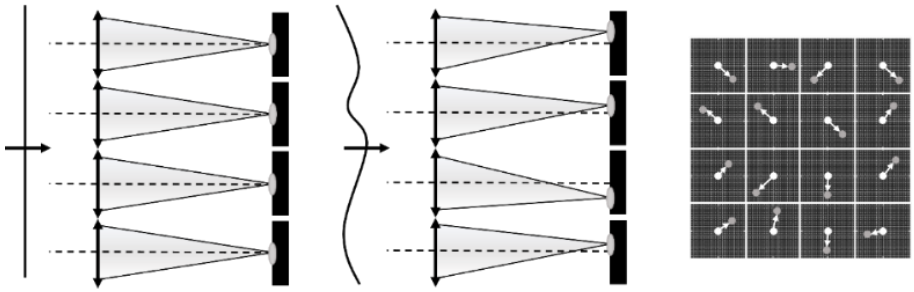

Figure 6: A SHWFS. Plane waves produce spots in their nominal positions (left). Distorted waves lead to spot translation (middle). Spot translation on a 2D array detector (right).

Other wavefront sensing solutions exist but are less common in adaptive optics systems. The pyramid wavefront sensor consists of a tip-tilt mirror, square-based prism placed at the focal plane, and imaging optics with an array detector which forms four images, one for each angled face of the prism. Modulating the path of the beam through the prism allows both the amplitude and sign of the phase derivative to be calculated via the distribution of light between the four images. The modulation requires physical manipulation of bulk optics, which is a large disadvantage [25], and must be tuned to balance dynamic range and sensitivity [26]. It has been shown to perform better than the SHWFS in diffraction-limited correction conditions, since the small subapertures in a SHWFS limit resolution more than the telescope aperture, though diffraction-limited conditions are rarely seen at the sensing wavelength [27].

One of the limitations of a SHWFS is the utilization of lenslets which imposes a fundamental limit on spatial resolution. This can be overcome by leveraging the near-field diffraction of small apertures. Yi et al. demonstrated this in an ultra-compact tilt-based wavefront sensor consisting of a square array of apertures fabricated on a CMOS

image sensor. The amount of power concentrated on each quadrant detector is proportional to incident angle due to diffraction at the aperture edges. This behaviour is monotonic up to 45° and enables high resolution tilt measurement for wavefront sensing [28].

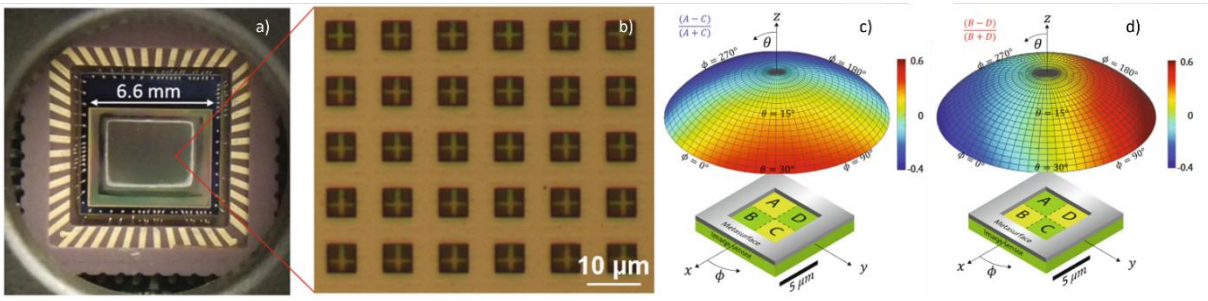

Figure 7: Tilt-based wavefront sensing based on the near fields of flat optics. Device architecture (a, b) and relationship between angle and power (c, d) [28].

It is possible to omit the wavefront sensor entirely in a technique called sensorless adaptive optics. Here the output of the system (e.g., optical fiber coupling efficiency) is used as a figure of merit to continuously optimize deformable mirror tuning through dithering. This reduces system complexity and allows all of the input light to theoretically be collected, however stability and speed are greatly reduced which is critical in the context of time-varying atmospheric turbulence [29]. The AO system approach using a SHWFS is ubiquitous due to its technical maturity and demonstrated success in astronomy and preliminary communication demonstrations. It may not however be the best solution for FSO considering speed, cost, and size. Silicon photonics can be leveraged to build an atmospheric turbulence mitigation solution on a single chip only a few millimetres in size, with much faster response time and lower power consumption. Specialized grating couplers like those developed in this work allow local

tip-tilt measurement to be performed directly on chip, meaning a Shack-Hartmann-like wavefront sensor can be integrated directly onto the chip.

Silicon Photonic Solutions

The field of silicon photonics has seen massive development over the last few decades and has a few key advantages over traditional platforms. One of the main benefits is its CMOS compatibility, enabling high throughput and low-cost production with mature processes and limiting the financial risk involved in investing in dedicated fabrication lines. The inherent nature of silicon presents some challenges, but developments in optical sources, modulators and detectors are making single-chip integrated solutions a reality [30]. The development of individual photonic components supports libraries of fully characterized and tested building blocks, leading to consistent performance, design flexibility and rapid prototyping at the device level [31]. Despite these advantages the industry is still currently in its infancy, with limited standardization between designers and foundries. As is the case with many scientific fields, record devices created in the context of research labs may not be compatible with existing commercial processes, limiting their utility. As we will see, improved performance may be found by using new materials, complex multilayer structures, and small feature sizes. Existing foundries provide a wide array of process parameters, and devices designed with fabricability in mind will lead to the greatest success [32]. Some commercially available foundries are presented in Table 1.

Table 1: A selection of various commercially available silicon photonic foundries [32].

Foundries (Platform)	MPW Platform	Wafer size (mm)	Film thickness (nm)	Process Line	Minimum CD (nm)	Typical MPW area (mm^2)
AMF (MPW)	SOI passive with heater	200	220nm Si	193nm	120	44.8
	PSIN-on-SOI passive with heater	200	220nm Si	248nm for SiN/ 193nm for Si	300 (SiN) / 120 (Si)	44.8
	SOI active	200	220nm Si	193nm	120	44.8
	PSIN-on-SOI active	200	400nm SiN 220nm Si	248nm for SiN/ 193nm for Si	300 (SiN) / 120 (Si)	44.8
AIM (MPW)	SOI	300	220	193nm (Immersion)	100	50
CEA-Leti (Si310-PHMP2M)	SOI	200	310	193nm	80	-
Cornerstone (MPW)	SOI	200	220/340/500	248 nm	200	56.2
GF (90WG)	SOI	300	170	193nm (Immersion)	90	25
IHP (SG25H5-ePIC)	SOI	200	220	248nm	-	10
IMEC (iSiPP50)	SOI	200	220	193nm	130	26.5
VTT (MPW)	SOI	150	3000	UV	-	50

The most common material platform in the industry is silicon on insulator (SOI) which is favoured for its high refractive index contrast leading to high confinement in structures with a small footprint. High contrast is also beneficial for devices like photonic crystals and grating couplers. Silicon nitride (SiN) has a lower index contrast but can achieve an order of magnitude lower loss behaviour due to a reduced dependence on waveguide sidewall roughness and can also be used at wavelengths below 1.1 μm because of its wider transmission window [33]. SOI has a much higher thermo-optic coefficient than SiN making it the preferred platform for thermo-optic phase shift tuning, though this makes SiN advantageous in temperature-sensitive applications [34]. Many current works use a combination of these two material platforms to take advantage of the benefits of each.

Phase shifters can be realized using many different architectures including thermo-optic, electro-optic, and micro electro-mechanical systems (MEMS). Phase shifters work by inducing a controllable variation in optical or physical path length resulting in an accumulation of phase in one signal relative to another. This can be accomplished by varying the effective index in a waveguide or by switching the optical route. Each architecture has advantages and disadvantages including speed, footprint, and power consumption. A thermo-optic phase shifter (TOPS) uses an integrated heating element to induce a refractive index change in a waveguide via the thermo-optic effect. This leads to a controllable optical path length difference. Though they are relatively low loss and are readily available in most commercial silicon photonic foundries, TOPS have a limited bandwidth under 100 kHz, limiting their utility in certain applications [35]. This is likely fast enough to compete with existing AO solutions such as the LCRD whose operating bandwidth is 20 kHz, and the low loss is beneficial for maximizing the signal-to-noise of the link.

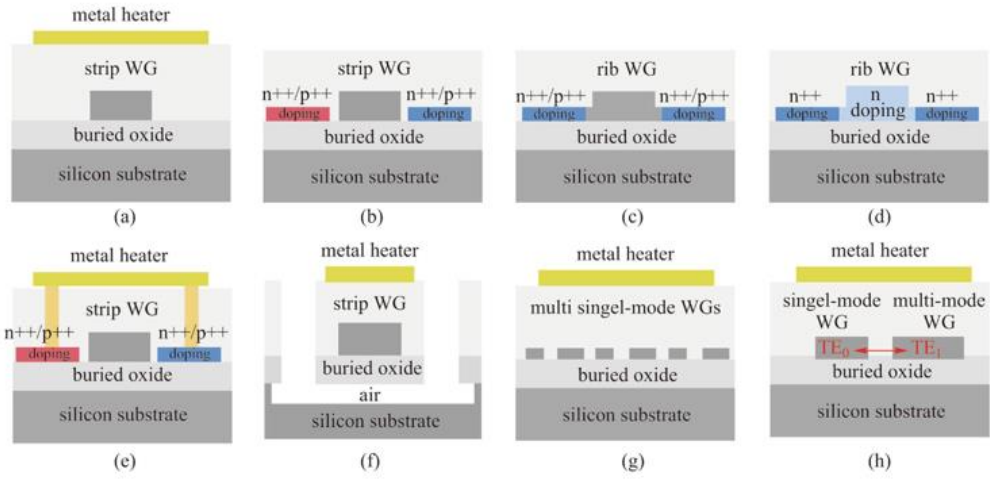

Figure 8: Various architectures of TOPS [35].

Carrier depletion phase shifters utilize changes in free carrier concentration controlled by a pn diode integrated into the waveguide to modulate phase. They have a greater modulation bandwidth in the GHz regime but experience higher insertion loss than TOPS and would be preferred in applications where the Greenwood frequency exceeds the bandwidth capabilities of TOPS [36].

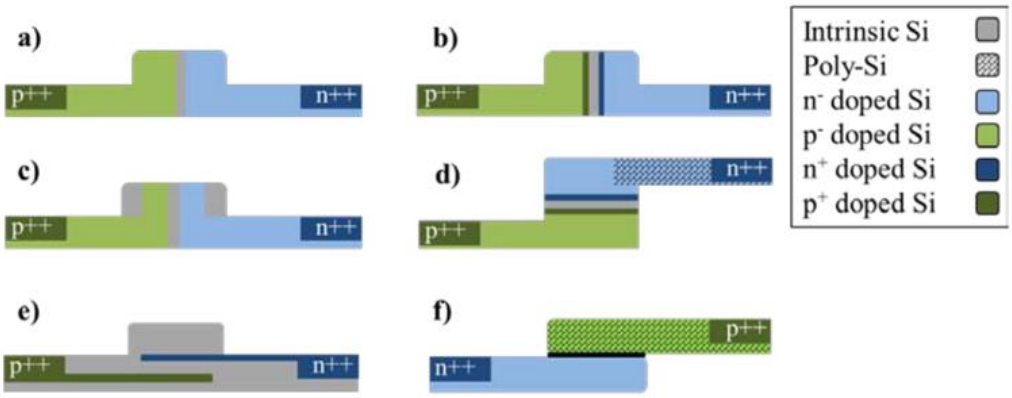

Figure 9: Various architectures of carrier depletion phase shifters [36].

MEMS are devices that incorporate both mechanical and electrical components onto a single platform. Phase shifting can be accomplished by modifying evanescent fields, changing the mode field distribution within the waveguide, or changing the path length [37]. Edinger et al. demonstrated a MEMS phase shifter using a suspended waveguide actuator that changes the effective index with proximity to the bus waveguide. This device is low loss and very power efficient, with an L_π of 17.2 μW and IL of 0.33 dB [38]. Despite this performance MEMS phase shifters are not currently available at commercial foundries due to their complexity and robustness issues. Either thermo-optic or carrier depletion phase shifters are preferred depending on the target bandwidth of the turbulence mitigation solution.

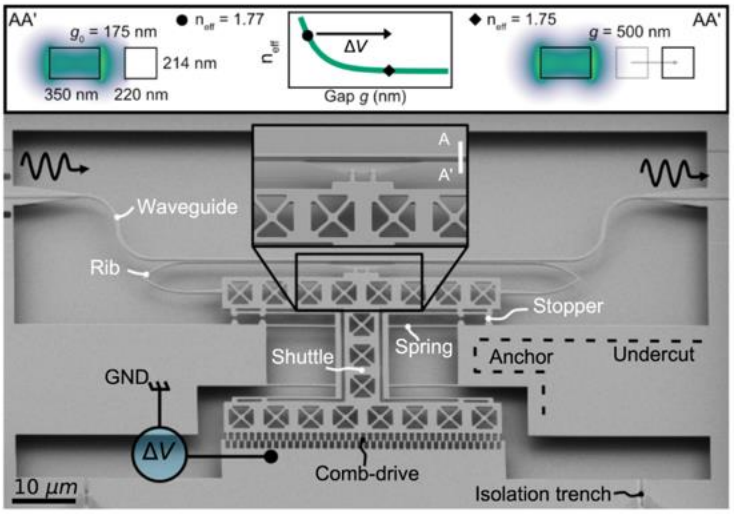

Figure 10: Suspended waveguide actuator MEMS phase shifter [38].

Photodetectors (PD) convert optical signals into electrical signals on chip and are crucial components in photonic systems. Various materials and structures exist including Ge on Si, heterogeneous III-Vs, and all-Si PDs. The best devices have low power consumption, high speed, small footprint, and are scalable with standard processing [39]. Devices based on Ge can be vertically grown directly on a Si waveguide. These have good speed and sensitivity but suffer from high dark current [40]. Though Si is not normally very absorptive at 1550 nm, monolithic Si PDs can be achieved using the deep-level states of lattice defects fabricated via ion implantation [41]. Devices based on III-V materials have been shown with efficiencies of 37% and generally outperform Si due to their direct bandgap nature but require more complex processing due to the lattice mismatch between III-V and Si [42].

Silicon photonics can perform wavefront correction, error estimation, and feedback analogous to an adaptive optics system or similar atmospheric turbulence mitigation

solution. Grating coupler arrays provide a collection interface between free space and the chip, phase shifters accomplish alignment between individual wavefront samples and photodetectors perform on-chip measurement. Systems can also be made optically "transparent" meaning the corrected wavefront can be output to a secondary system instead of being measured on-chip, where more mature off-chip technologies can be leveraged for detection.

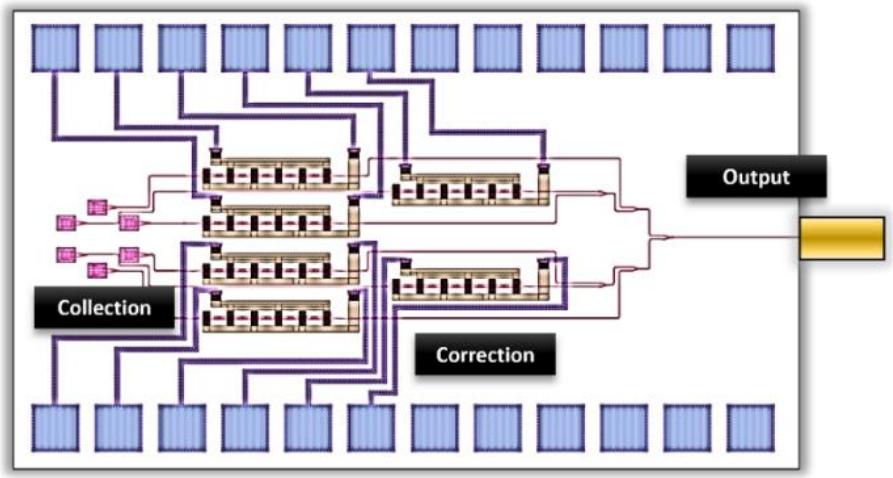

Figure 11: Schematic of a silicon photonic based wavefront correction system.

Using silicon photonics as a free space optical interface has been demonstrated for a variety of applications. The grating coupler array architecture described here is a common solution in optical phased array (OPA) applications including LiDAR, holographic displays, orbital angular momentum (OAM) mode generation, and free space optical communication links. An OPA uses an array of emitters with individual phase control to modulate the pattern of an emitted far-field beam. The far-field pattern can be modified by tuning the phase of each individual element with integrated phase-shifters,

enabling tunable modes and beam steering. These devices are often designed with emission characteristics in mind, rather than collection performance.

OPAs operating at 1550 nm are an exciting technology for LiDAR in autonomous vehicles (AVs). LiDAR has been shown to outperform RADAR, ultrasonic sensing, and IR cameras in terms of field of view, longitudinal accuracy, and lateral resolution. Silicon photonic-based OPAs have many advantages over mechanically rotating scanning LiDAR including higher speed, lower power consumption, smaller form factor, and robustness [43]. Holographic projectors for head-mounted augmented reality applications have been demonstrated using visible-light OPAs fabricated with a CMOS-compatible process. This platform has advantages over bulk optics approaches including compact form factor, daytime operation, and full-depth projection to reduce eye fatigue. An OPA design by Notaros et al. utilizes pixel tuning in both amplitude and phase on a transparent platform [44].

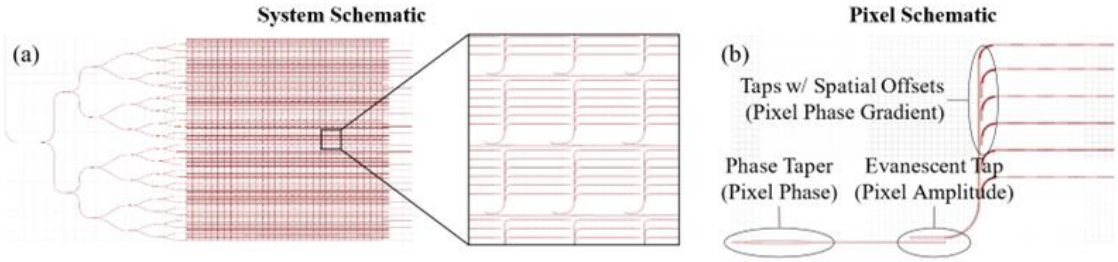

Figure 12: OPA for holographic projection implemented on a transparent platform [44].

Poulton et al. have demonstrated chip-to-chip FSO communication using transmitting and receiving OPAs achieving a 10 Gbps data rate over a 50 m lens-free optical link. They

also demonstrated a reconfigurable point-to-multipoint network using a single active OPA transmitter aligned to two passive OPA receivers in sequence with a 1 Gbps data rate per channel [45]. The OPAs in this work were also used for a LiDAR application in which phase tuning provides angle control in one dimension and wavelength tuning provides control in the second dimension. This architecture has the benefit of requiring orders of magnitude fewer phase-shifting components reducing I/O count and power consumption, however it increases system complexity due to the tunable source.

Grating Couplers

Grating couplers are nanophotonic devices that utilize structures of varying refractive index to diffract light from a free-space mode to an on-chip waveguide mode and are critical to overall system performance. One of the most important considerations in an optical communication link is loss, and it is therefore crucial to optimize grating coupler design for total coupling onto the chip at the target wavelengths. The realizable coupling efficiency of a coupler design is limited by fabrication constraints which dictate material choice, layer thickness, minimum feature size, and process uniformity. Coupling efficiencies over 70% have been reported for vertical incidence [46]. Notaros et al. have demonstrated grating couplers with a theoretical efficiency of 95% and measured efficiency of 92% using a commercially available CMOS process, an impressive result that validates the usage of existing CMOS technology for photonic applications [47].

One common application of grating couplers is coupling light between a photonic chip and optical fiber which requires good modal overlap between the grating and fiber. In

emission, a uniform grating has an exponential scattering profile which does not match the Gaussian profile of a standard fiber. This mismatch is a source of loss that sets an upper theoretical efficiency bound of 80% [48]. Modifying the fill factor and period of the grating along its length changes the scattering strength as a function of distance and alters the emission profile to provide better mode matching, a technique called apodization. Zhao et al. have demonstrated an apodization design algorithm that predicts a grating to fiber coupling efficiency of 61.4%, which is competitive with other much more sophisticated design techniques [49]. Apodization could also be used to design gratings for target emission profiles other than a Gaussian.

A second source of loss is the scattering of light downward into the substrate where it dissipates and is not collected by the fiber. Various types of bottom reflectors have been designed to redirect this light back into vertical emission providing substantial gains in coupling efficiency. Van Laere et al. used a polymer buffer layer and underside gold mirror to increase the theoretical efficiency of their coupler from 30% to 72% with a measured efficiency of 69%. The increase in performance comes at the cost of several post processing steps including polymer spin coating and curing, wet chemical etching of the original Si substrate, and fabrication of the gold mirror [50]. A more scalable solution compatible with the CMOS process is to use dielectric distributed Bragg reflectors (DBR) as demonstrated by Zhang et al. using alternating layers of amorphous Si and SiO_2. The reflectivity of their structure exceeds 94% over a broad wavelength range from 1400 nm to 1600 nm and demonstrates high tolerance to layer thickness variation [51].

Subwavelength gratings (SWG) have feature sizes smaller than the wavelength of light and behave as homogenous media with an effective index determined by structure and material composition. They are emerging as effective tools to tune device performance in applications such as Bragg gratings, ring resonators, and grating couplers [52]. Compact bi-wavelength grating couplers can be designed using effective index tuning to satisfy the coupling condition at two distinct wavelengths with orthogonal polarizations. This enables compact devices with a single output port and eliminates the need for very broadband gratings in this application. Such a device was demonstrated by Cheng et al. who also designed a SWG diplexer to separate the two wavelengths on chip [53].

The operation of a grating coupler relies on the principle of diffraction, which is inherently angle dependent. Fiber alignment loss is therefore a common issue but can be mitigated with certain coupler designs. Ding et al. demonstrated an 18 nm coupling peak shift for a 2° shift in incident angle for their coupler design [54].

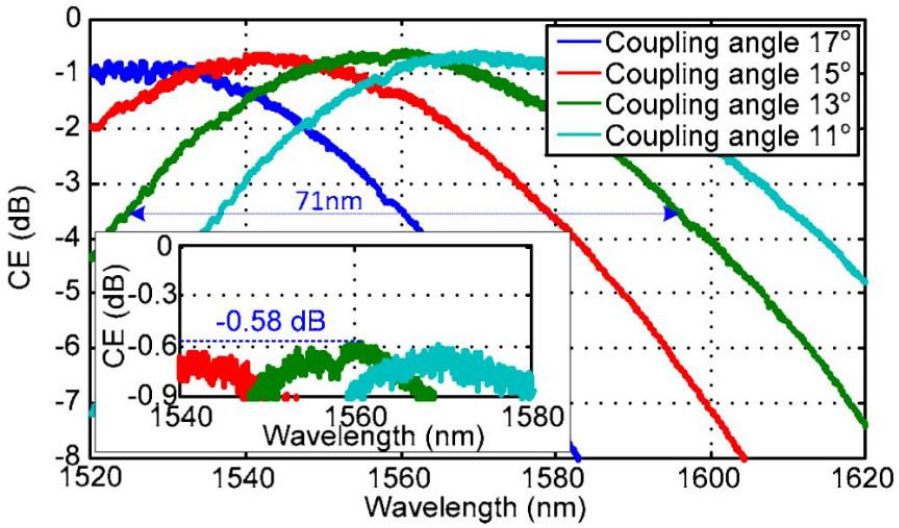

Figure 13: Demonstration of a shift in coupling peak with incident angle [54].

Polarization of the incident beam also affects coupling efficiency. For fiber coupling applications using standard single mode fiber the input polarization is generally not known or stable over time due to fluctuations in the fiber birefringence from temperature variation and mechanical stress. A polarization diversity coupler mitigates this issue by decomposing the input signal into two independently collected orthogonal states. The total light collected will remain constant, although the proportion of signal in each output will depend on the input polarization [55]. Many of these designs utilize a 2D grating coupler structure with square symmetry and outputs placed at 90° to each other. Each input basis polarization is coupled to the TE mode of an independent orthogonal waveguide which can then be recombined, making on-chip polarization conversion unnecessary [56]. In a separate application the polarization-sensitive nature of grating couplers has been leveraged to design on-chip Stokes polarimeters which fully characterize the polarization of an input beam. By splitting the input into two orthogonal polarization components using a 2D grating and recombining them into four outputs on chip, the input polarization state can be computed from the power distribution between the four outputs [57].

The characteristic length of most grating couplers is tens of microns which matches the mode field diameter of the optical fibers they are often paired with. However, the standard size of a low-loss single mode silicon photonic waveguide is just 500 nm. Waveguide tapers must be used to convert the large grating mode to the smaller waveguide mode with low loss. Adiabatic taper designs can accomplish this but are hundreds of microns long, taking up valuable chip footprint. A potential solution is to use

focusing grating couplers which utilize curved gratings to produce cylindrical wavefronts. These can be focused to a waveguide mode, reducing the length of the taper to a few tens of microns [58]. A 2D focusing grating can be made via the superposition of two orthogonal focusing gratings forming a compact polarization diversity grating coupler as in [59].

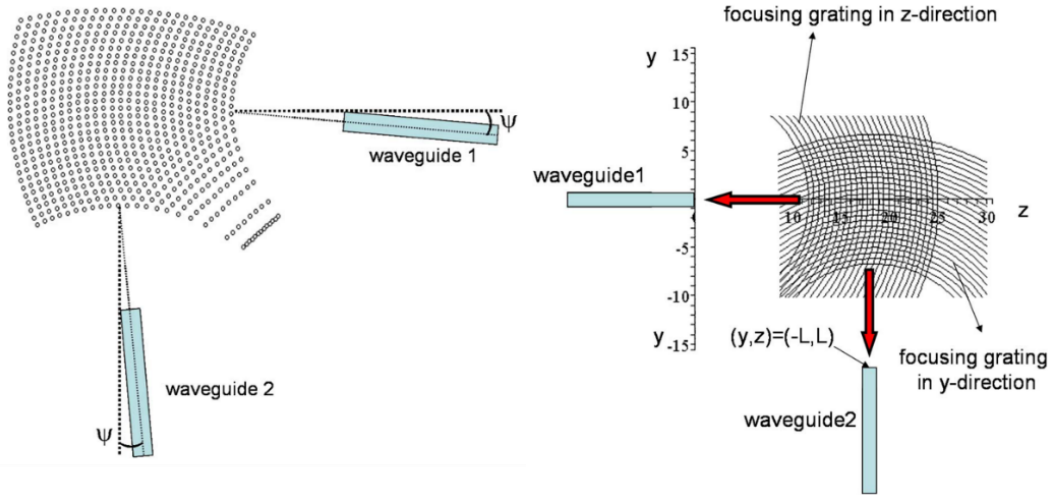

Figure 14: 2D focusing grating formed by the superposition of two curved elliptical gratings [59].

Nanophotonic Design Optimization

The design of grating couplers is fundamentally an optimization problem, with a well-defined set of design variables, objectives, and constraints. In essentially all applications, analyzing every possible solution in a design space is not feasible due to the vast number of combinations and resource-intensive process of performance verification. More efficient optimization methodologies exist and have been implemented in nanophotonic design including genetic algorithm, particle swarm, and inverse design techniques, each with their own advantages and disadvantages.

Genetic Algorithms use the ideas of natural selection to evolve candidate designs towards better solutions. Initial randomly generated designs are analyzed for fitness using a figure of merit. Subsequent designs are created by combining characteristics from the best designs in each generation. Some additional random modifications (mutations) can be included to better characterize the entirety of the global design space. Though this technique is generally successful in finding global maxima this is not guaranteed, and convergence is slow requiring many iterations [60]. Covey and Chen demonstrated a perfectly vertical fiber to chip grating coupler with a simulated efficiency of 68% and measured efficiency of 60.1% designed using a genetic algorithm. They analyzed fabricated structures' layer thicknesses and etching errors to modify their algorithm, eventually producing designs very robust to fabrication tolerances [61].

In Particle Swarm optimization, a set of designs is randomly generated at different points and velocities within the design space. A particle's point defines its current set of design parameters, and its velocity describes the magnitude and direction of that particle's movement through the design space at each optimization iteration. Each particle is evaluated with a figure of merit and updated to a new position according to its velocity, which is updated via a tunable algorithm which considers the global best position, particle's previous best position, and previous velocity. In this way the particles step through the design space at each iteration and converge to an optimal design. A randomness parameter can be added to the velocity of each particle to increase the likelihood of finding a global maximum [62].

The inverse design process reverse engineers a structure based on a target figure of merit and optimization procedure instead of analytically using known physics. It can provide faster convergence and good performance even though it often results in non-intuitive designs. A common approach is to use the adjoint method, which uses a forward and adjoint (reverse) simulation to compute the gradients of a set of design variables with respect to a figure of merit. Each design variable is then modified according to its gradient, producing the subsequent iteration. The design variables may be a set of parameters describing a shape, using a polynomial for example, or a grid of pixels each representing a specific material topology. This topology optimization has been recently used to design many different types of components including splitters, multimode interferometers, and grating couplers. Hammond et al. demonstrated a polarization-splitting grating coupler using a dual layer structure with SOI bottom layer with a poly-Si overlay. Each layer was topologically designed for operation at 1550 nm [63]. Upon fabrication the authors note a 1.4 dB increase in insertion loss and 28 nm shift in centre wavelength, likely due to the complexity of the dual layer fabrication process which magnifies the effect of small features often seen in topology optimization. Adjoint-based optimization scales independently of the number of degrees of freedom, making it a particularly attractive and flexible choice for nanophotonic components [64].

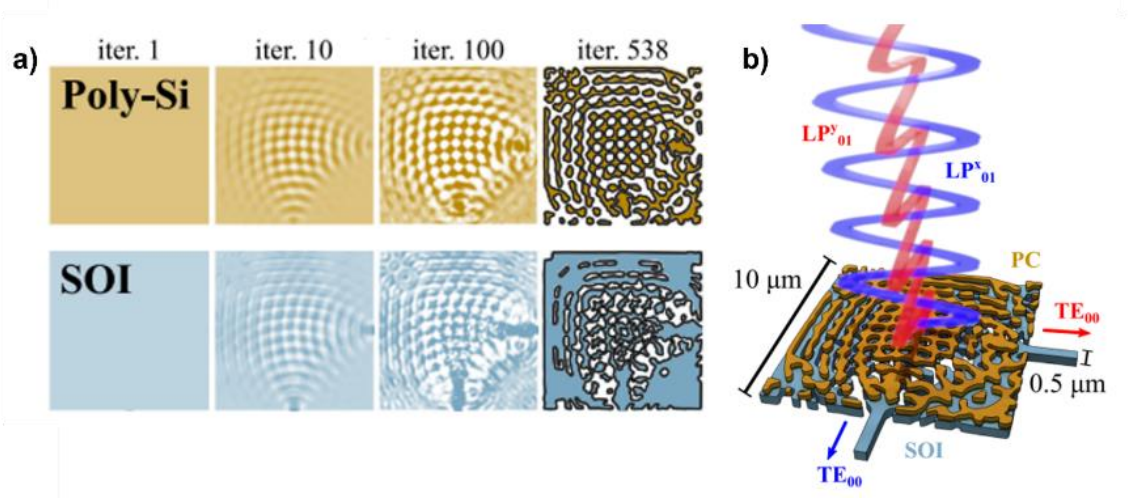

Figure 15: A dual-layer 2D grating coupler designed by topology optimization. Iterative refinement of the design (a), final device structure (b) [63].

Michaels and Yablonovitch used adjoint-based shape optimization to design a vertical grating coupler with a simulated coupling efficiency of 99.2%. Their two-layer structure creates constructive and destructive interference between the top and bottom layers to significantly reduce back reflections and scattering into the substrate producing high directionality. Only 67 iterations of their algorithm were needed to converge to this design, taking only two hours of computation, highlighting the power of the adjoint inverse design technique [65].

An interesting byproduct of these techniques is the partial removal of the designer's intuition from the design process. It may not be initially clear how an optimized structure is fundamentally operating. An example of this is the vertical grating coupler work of Covey and Chen. One optimized design consisted of four stages, an initial apodized region, a second main emission region, a third chirped region providing angled emission towards the fiber, and a fourth quasi-periodic Bragg reflector region. These features were

not intentionally defined but were the result of the optimization. When the designers replaced the fourth stage with a uniform Bragg reflector with much higher reflectivity in an attempt to improve performance, the overall coupling decreased by 6%. Part of the original reflector region was found to emit side-lobes that interact with other areas of the grating improving efficiency, something the designers did not intuitively expect [61].

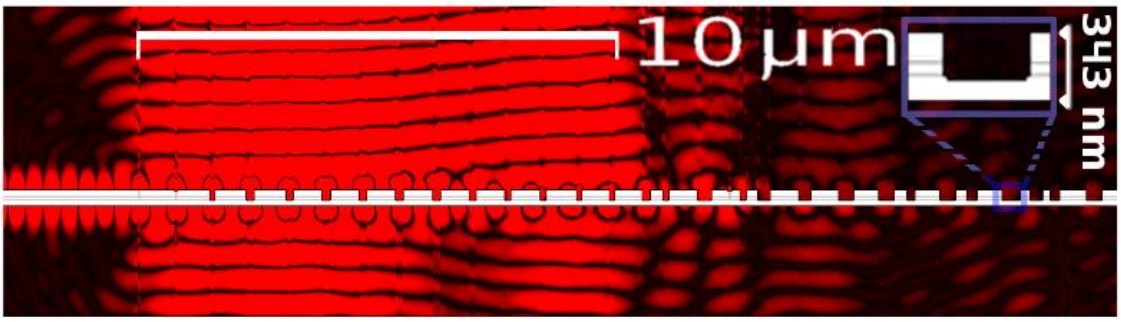

Figure 16: Vertical coupler designed by Covey and Chen showing the complex radiation pattern along the grating. Many optimization schemes lead to superior performance but not intuitive designs [61].

Background Theory

Grating Coupler Operation

The working principle of grating couplers is based on the diffraction of light. Diffraction occurs when a propagating wavefront encounters a feature similar in size to its wavelength, producing spherical wavelets. Wavelets originating at different points will interfere with each other constructively or destructively depending on the relationship between wavelength and optical path length, producing a pattern of varying intensity. Diffraction occurs in all types of propagating waves and can be easily seen in the interference of ripples in a pool of water.

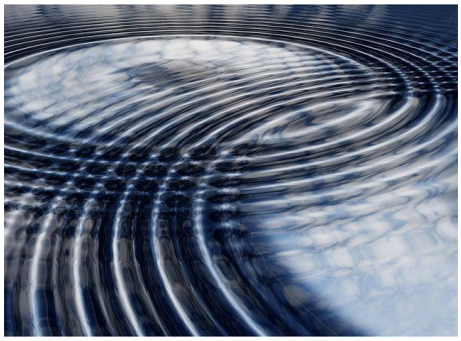

Figure 17: Diffraction phenomena are easily visible in the interaction of water ripples.

The specific pattern produced by diffraction depends on the structure causing the interference, meaning carefully designed structures can be engineered for various applications including silicon photonics. A photonic grating consists of a periodic structure with wavelength-scale feature size containing at least two materials with

differing refractive index. When light is incident on this structure the refractive index contrast modifies the field to match the grating periodicity resulting in diffraction into a set of allowed modes. These allowed modes are governed by the phase-matching condition which forces the resultant fields to be continuous. In other words, the wavevector of the incident light must match the wavevector of the transmitted and reflected modes modified by the grating. For each mode m,

$$\boldsymbol{k_m} = \boldsymbol{k_{inc}} - m\boldsymbol{G} \tag{1}$$

where $\boldsymbol{G}$ is the grating vector. Expanding gives

$$\frac{2\pi}{\lambda} n_{eff} \sin\theta_m = \frac{2\pi}{\lambda} n_{inc} \sin\theta_{inc} - m\frac{2\pi}{\Lambda} \tag{2}$$

where λ is the wavelength of light, n_{eff} is the effective index of the grating, θ_m is the diffracted mode angle, θ_{inc} is the incident angle and Λ is the periodicity of the grating.

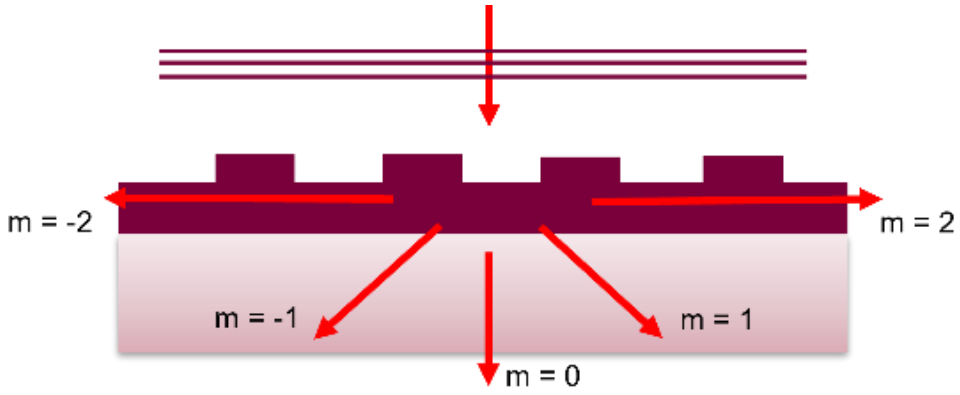

Figure 18: A plane wave splits into diffracted modes on propagation through a diffraction grating.

Photonic grating couplers use specially designed gratings to couple light from free space into a guided mode on chip. Guided modes are those supported by the output waveguide

and are defined by the refractive index contrast of the core and cladding materials as well as the geometry. In a ray tracing context, the allowed modes are those where the angle of total internal reflection results in constructive interference in the direction of propagation. Other angles result in radiative modes that leak power into the surrounding cladding.

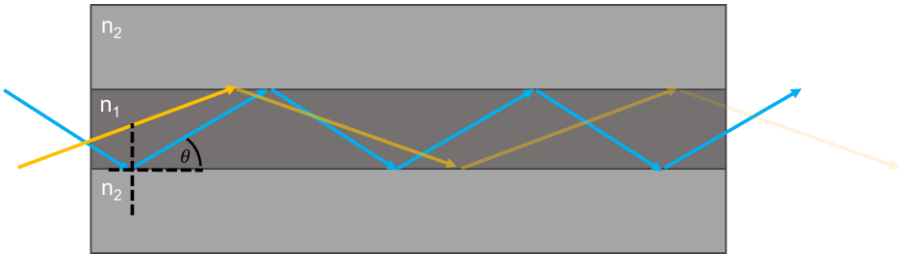

Figure 19: The ray tracing approximation of waveguide modes. Some angles allow propagation (blue) while others radiate to the cladding (yellow).

Each guided mode has a corresponding propagation constant defined as:

$$\beta = k_0 n_{eff} = k_0 n \sin\theta \tag{3}$$

where θ is the angle of total internal reflection. If the Bragg phase-matching condition between the wavevector of the diffracted mode and propagation constant of a guided mode is satisfied, then that guided mode is allowed and will experience gain. To satisfy the Bragg condition a designer must therefore choose an appropriate grating for a given wavelength, incident angle and waveguide design to excite guided modes and achieve coupling. Though the Bragg condition predicts which modes are allowed, it does not predict the amount of coupling into each one. Further analysis must be done to design a coupler with desired performance, often using a numerical approximation technique such as the Finite-Difference Time Domain (FDTD) method.

A further consideration affecting coupling is the mode mismatch between the guided mode in the grating area and the guided mode in the routing waveguide. Ideally, the effective indices of these two regions will match exactly to minimize loss. Once the grating period is chosen for phase-matching the effective index of the grating can be tuned by changing the fill factor of the grating. The interplay between these two effects along with the non-quantifiable power distribution between diffracted modes are the main reasons analytic designs are only approximate.

FDTD Analysis

Maxwell's Equations

The FDTD method is a numerical technique for solving time-dependent systems of partial differential equations by discretizing each variable spatially then calculating their evolution over discrete time steps. The laws governing the behaviour of light form such a system and are described by Maxwell's equations.

$$\nabla \cdot \boldsymbol{D} = \rho_V \tag{4}$$

$$\nabla \cdot \boldsymbol{B} = 0 \tag{5}$$

$$\nabla \times \boldsymbol{E} = -\frac{\partial \boldsymbol{B}}{\partial t} \tag{6}$$

$$\nabla \times \boldsymbol{H} = \frac{\partial \boldsymbol{D}}{\partial t} + \boldsymbol{J} \tag{7}$$

The last two equations describe time-dependent coupling between currents, electric fields, and magnetic fields and are the only two necessary to describe electromagnetic propagation using FDTD analysis [66], [67]. The quantities $\boldsymbol{D}$ and $\boldsymbol{B}$ represent the

electric and magnetic displacement fields which describe the microscopic behaviour of bound charge and current. They are related to the macroscopic electric field $\boldsymbol{E}$ and magnetic field $\boldsymbol{B}$ through the constitutive relations, which for linear, isotropic media can be written as

$$\boldsymbol{E} = \frac{1}{\epsilon}\boldsymbol{D} \tag{8}$$

$$\boldsymbol{H} = \frac{1}{\mu}\boldsymbol{B} \tag{9}$$

where ϵ and μ are the permittivity and permeability of the material. Substituting gives

$$\frac{\partial \boldsymbol{E}}{\partial t} = \frac{1}{\epsilon}\nabla \times \boldsymbol{H} \tag{10}$$

$$\frac{\partial \boldsymbol{H}}{\partial t} = -\frac{1}{\epsilon}\nabla \times \boldsymbol{E} \tag{11}$$

for lossless and source-free space.

In Two Dimensions

Simulating in 2D can have advantages over full 3D simulation in terms of complexity and speed. In this case the entire structure is treated as infinite along the third dimension, which removes terms from the coupled equations partially decoupling them into two modes. For the transverse electric (TE) mode, defined as the mode with electric field components perpendicular to the direction of propagation, the relevant fields are written as

$$\frac{\partial E_y}{\partial t} = \frac{1}{\epsilon}\left(\frac{\partial H_x}{\partial z} - \frac{\partial H_z}{\partial z}\right) \tag{12}$$

$$\frac{\partial H_x}{\partial t} = \frac{1}{\mu_0}\frac{\partial E_y}{\partial z} \tag{13}$$

$$\frac{\partial H_z}{\partial t} = -\frac{1}{\mu_0}\frac{\partial E_y}{\partial x} \tag{14}$$

These equations are spatially discretized along a grid defined by the 2D Yee cell which interleaves central finite difference calculations for each of the three fields.

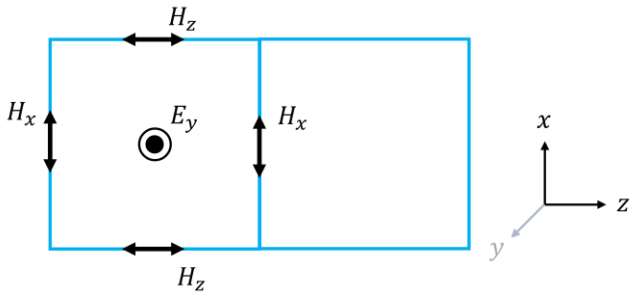

Figure 20: The 2D Yee cell.

$$E_y^n(i,k) = E_y^{n-1}(i,k) + \frac{\Delta t}{\epsilon \Delta z}\left(H_x^{n-\frac{1}{2}}\left(i,k+\frac{1}{2}\right) - H_x^{n-\frac{1}{2}}\left(i,k-\frac{1}{2}\right)\right) - \frac{\Delta t}{\epsilon \Delta x}\left(H_z^{n-\frac{1}{2}}\left(i+\frac{1}{2},k\right) - H_z^{n-\frac{1}{2}}\left(i-\frac{1}{2},k\right)\right) \tag{15}$$

$$H_x^{n+\frac{1}{2}}\left(i,k+\frac{1}{2}\right) = H_x^{n-\frac{1}{2}}\left(i,k+\frac{1}{2}\right) + \frac{\Delta t}{\mu_0 \Delta z}\left(E_y^n(i,k+1) - E_y^n(i,k)\right) \tag{16}$$

$$H_z^{n+\frac{1}{2}}\left(i+\frac{1}{2},k\right) = H_z^{n-\frac{1}{2}}\left(i+\frac{1}{2},k\right) - \frac{\Delta t}{\mu_0 \Delta x}\left(E_y^n(i+1,k) - E_y^n(i,k)\right) \tag{17}$$

Here n represents discrete time steps, i is the Yee cell along the x-axis and k is the Yee cell along the z-axis. A similar analysis can be followed to simulate structures in one or three dimensions [68].

Topology Optimization

Topology optimization (TO) is a technique that maximizes the performance of a device by modifying the structure and material composition within a defined design space for a given set of constraints and design objectives. The design space is divided into an array of pixels, each representing a unique design variable. Because of this formulation, the final design can take on many different shapes and is not constrained by predefined configurations based on a smaller set of design parameters. Aside from photonics, TO also has applications in other engineering disciplines including mechanical and civil engineering.

In nanophotonic TO the goal is to create an arrangement of materials with favourable scattering and guiding characteristics for the target application. It can be implemented in commercial FDTD solvers allowing users to easily define sources, figures of merit and design regions. Each step of the iteration is computed using the adjoint method which normally requires only two simulations, one forward and one adjoint. This can be accomplished following the formulation detailed in [69]. For a design region defined as a function of x, the change in the figure of merit at a specific point x_0 induced by a slight change in permittivity is:

$$\Delta FoM = Re\left[\overline{\boldsymbol{E}^{\boldsymbol{old}}(x_0)} \cdot \boldsymbol{\Delta E}(x_0)\right] \tag{18}$$

where $\boldsymbol{E}^{\boldsymbol{old}}(x_0)$ is the electric field before the change is made and $\boldsymbol{\Delta E}(x_0)$ is the change in electric field that occurs due to the permittivity alteration. We can write this change in electric field as a function of the new electric field using the Maxwell Green's function

which relates the electric field at x_0 to the induced polarization density, $\boldsymbol{p^{ind}}$, over a small volume ΔV.

$$\boldsymbol{\Delta E}(x) = \overline{\overline{\boldsymbol{G^{EP}}}}(x_0, x)\boldsymbol{p^{ind}} \tag{19}$$

$$\boldsymbol{\Delta E}(x) = \epsilon_0 \Delta\epsilon_r \Delta V \overline{\overline{\boldsymbol{G^{EP}}}}(x_0, x)\boldsymbol{E^{new}}(x) \tag{20}$$

Here $\Delta\epsilon$ is the change in permittivity due a small change in the design for the current optimization iteration. For a small enough change in the design, we can say that the new electric field will be approximately the same as the old electric field, allowing us to make a substitution. Rearranging (18) for the change in the figure of merit with respect to the change in permittivity gives:

$$\frac{\Delta FoM}{\Delta\epsilon_r} = \epsilon_0 \Delta V \mathrm{Re}\left[\overline{\boldsymbol{E^{old}}(x_0)} \cdot \left(\overline{\overline{\boldsymbol{G^{EP}}}}(x_0, x)\boldsymbol{E^{old}}(x)\right)\right] \tag{21}$$

Rewriting (27) using the reciprocity of the Green's function allows us to represent the change in the figure of merit with respect to the change in permittivity as a function of just two electric field distributions, one of which can be calculated from a forwards simulation and the other from an adjoint simulation.

$$\frac{\Delta FoM}{\Delta\epsilon_r} = \mathrm{Re}\left[\left(\epsilon_0 \Delta V \overline{\overline{\boldsymbol{G^{EP}}}}(x, x_0)\overline{\boldsymbol{E^{old}}(x_0)}\right) \cdot \boldsymbol{E^{old}}(x)\right] \tag{22}$$

$$\frac{\Delta FoM}{\Delta\epsilon_r} = \mathrm{Re}\left[\boldsymbol{E^{adj}}(x) \cdot \boldsymbol{E^{old}}(x)\right] \tag{23}$$

The adjoint simulation treats the point x_0 as a dipole emitter driven with amplitude $\Delta V \epsilon_0 \overline{\boldsymbol{E^{old}}(x_0)}$. The calculated gradient of the figure of merit is used to modify the permittivity at each point in the design region using a gradient descent method. The

design tends towards an optimum by tuning each design parameter at every step in the process, usually leading to faster convergence and higher final figures of merit.

The TO in this work is implemented using Meep, a free and open-source python-based EM FDTD solver [70]. It was chosen for its configurability and ready-to-use packages that implement the adjoint method and gradient descent optimization. It was used to optimize waveguide tapers leading from the grating coupler collection area to output waveguide which has a much smaller mode size. The figure of merit maximizes the proportion of light from the input waveguide fundamental mode to the output waveguide fundamental mode.

Methods

The goal of this work is to create a four-arm grating coupler capable of measuring incident angle. An array of these devices would give local phase estimation via a reconstruction algorithm, allowing wavefront errors to be corrected using an AO system or silicon photonic solution.

The Bragg condition shows that the guided modes of a given grating coupler depend on incident angle and wavelength. Often, grating coupler applications require a specific incident angle to accept light from standardized components such as optical fibers. This makes incident angle a design constraint for the grating since changing the incident angle causes a shift in the spectrum of allowed guided modes, leading to losses at the design wavelength and gains at adjacent wavelengths. Grating couplers therefore have a limited angle tolerance over which performance is within specification. Grating couplers and waveguides are also inherently polarization dependent leading to polarization dependent loss when collecting a signal with an unknown or time-varying polarization.

Commonly, the effects of incident angle and polarization are detrimental to system performance and designers attempt to limit their impact as much as possible. However, a grating coupler with known angle and polarization dependencies could be used as a measurement device as long as the relationship between the measurements and calculated parameters is invertible. Analyzing the power in four outputs of a 2D grating coupler provides enough information to fully compute an input beam's incident angle and

polarization through monotonic relationships. A 2D array of these devices allows local estimation of the tip and tilt angles, and illuminating such a device with a distorted wavefront therefore provides local phase estimation of the distortion, analogous to a SHWFS. This device is an integrated silicon photonic wavefront sensor.

The wavevector of an incident beam can be expressed in terms of two spatial angles (α, β) and one polarization angle (ϕ). These angles can be computed from the power coupled into each of the four output ports labeled UP, DOWN, LEFT, and RIGHT.

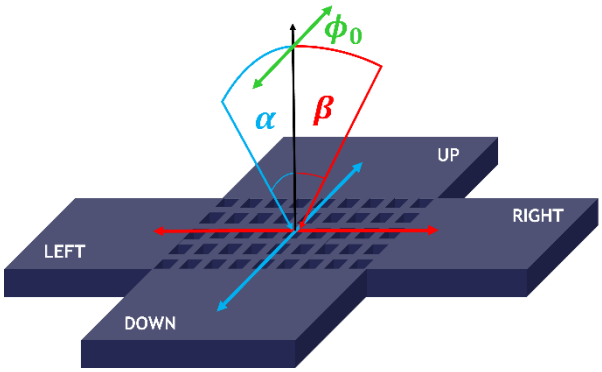

Figure 21: Visualization of the two spatial angles (α, β) and polarization angle (ϕ) that define an incoming wavefront.

The monotonic relations for small angles are as follows:

$$\alpha \propto \frac{T_{UP} - T_{DOWN}}{T_{UP} + T_{DOWN}} \tag{24}$$

$$\beta \propto \frac{T_{LEFT} - T_{RIGHT}}{T_{LEFT} + T_{RIGHT}} \tag{25}$$

$$\phi_0 \propto \frac{(T_{UP} + T_{DOWN}) - (T_{LEFT} + T_{RIGHT})}{T_{UP} + T_{DOWN} + T_{LEFT} + T_{RIGHT}} \tag{26}$$

A similar relationship also holds in two dimensions for 1D grating couplers, where the relationship for β still holds.

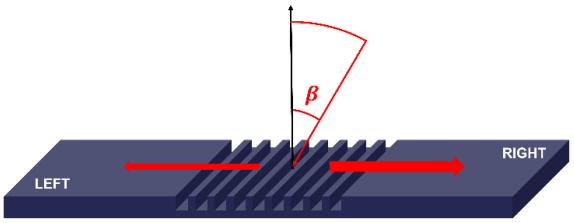

Figure 22: Tilt in one dimension can be measured using a two-arm grating.

To allow computation of the incident angle the 2D grating coupler must produce a monotonic relationship between incident angle and output power over the desired angle range at the carrier wavelength. In other words, each set of incident angles must produce a unique set of output parameters. This can be realized by designing the grating for a target peak shape and angle-induced spectrum shift. Figure 23 shows a set of grating coupler transmission spectra for a single design at different incident angles. The peak shape does not vary, however the peak shifts to shorter wavelengths with increasing angle. This is in accordance with the phase-matching condition. The figure inset shows the relationship between angle and transmission at a hypothetical target wavelength of 1470 nm. The relationship is monotonic under these operating conditions and would therefore facilitate tilt measurement.

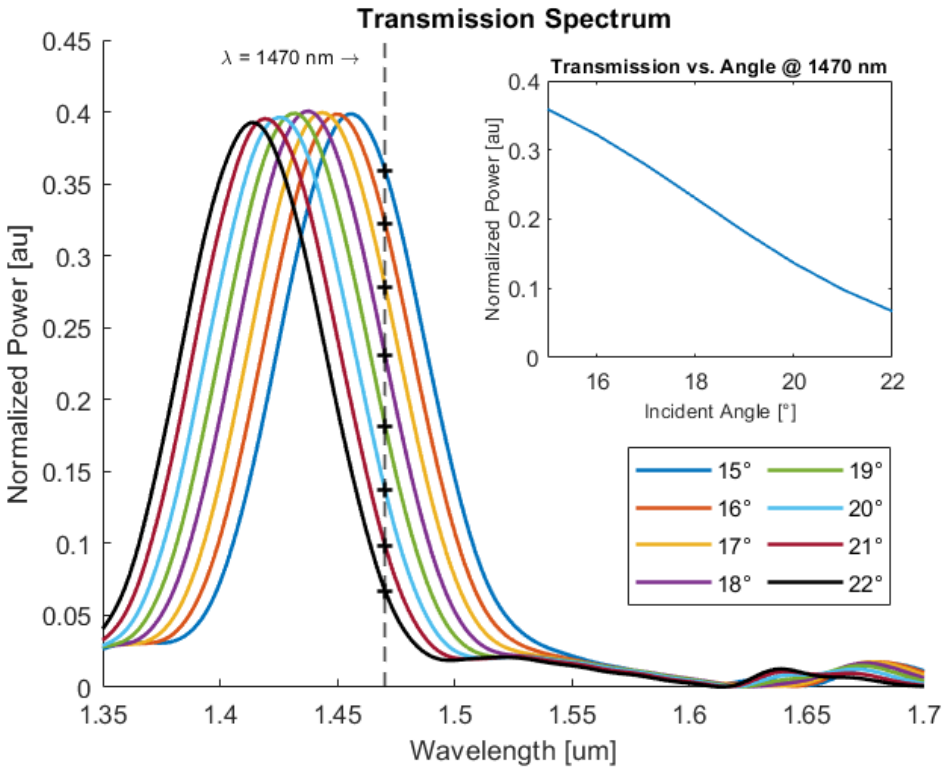

Figure 23: Transmission spectrum shift with changing incident angle. This produces a monotonic relationship between coupling and angle at the target wavelength.

Initial Design

The design of the grating couplers in this work is constrained by fabrication process parameters. All fabrication is done by the Applied Nanotools Inc. (ANT) NanoSOI fabrication process featuring 220 nm device Si layer, 2000 nm buried SiO_2 (BOX) layer, and 2200 nm top SiO_2 (TOX) cladding. Features are defined using 100 keV electron beam lithography (EBL) and reactive ion etching (RIE) with a minimum feature size of 60 nm and full-depth etching [71]. This process was chosen for its rapid turnaround time and small feature size, though the absence of multilayer etching imposes a fundamental limit on device performance.

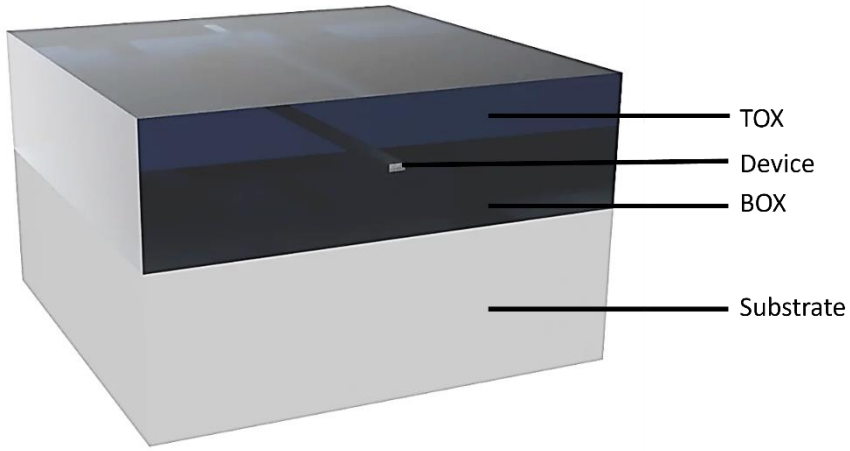

Figure 24: ANT process cross section showing different layers [71].

A simple uniform grating coupler can be designed with these constraints. The structure is defined by two parameters, the grating period and fill factor. Period defines the length of each grating unit cell and fill factor defines the proportion of that period that is not etched. The values of these grating parameters determine the grating coupler efficiency and operating wavelength.

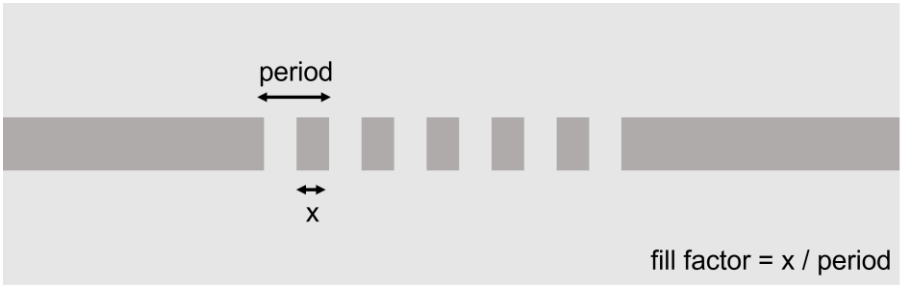

Figure 25: A simple uniform grating can be defined by two parameters, period, and fill factor.

Four-arm gratings can be created from these 2D designs by using a uniform nanohole structure where the spacing of the nanoholes is the period and the radius of the etched areas is defined by the fill factor. It is assumed that the 2D design process will have a

strong correlation to the 3D geometry since the cross section of the nanohole array is identical to the 2D grating.

Analytic Approximation

Period and Fill Factor

The first step in the design process is to analytically determine a good starting point based on the Bragg phase-matching condition. A grating coupler with uniform periodicity is designed for a target wavelength of 1550 nm at vertical incidence to match expected operating conditions. Using the Bragg condition, the grating coupler period is

$$\Lambda = \frac{\lambda}{n_{eff}} \tag{27}$$

for vertical incidence where λ is the wavelength and n_{eff} is the effective index of the grating. The effective index of the grating depends on the effective indices of the etched, n_{eff1}, and non-etched, n_{eff2}, regions and the fill factor:

$$n_{eff} = ff \times n_{eff1} + (1 - ff) \times n_{eff2} \tag{28}$$

There are two methods used to calculate the effective indices. Both use a slab waveguide methodology, which models confinement in only one dimension and treats the other as infinite. This assumption holds as the width of the grating coupler is approximately ten times the wavelength or greater, and there are minimal confinement effects. MATLAB code adapted from [72] and based on [73] gives one estimate. The second method is described in [74].

A set of potential grating designs is then calculated resulting in various combinations of period and fill factor. Each effective index calculation method gives a slightly different result, but in general they are in close agreement. These sets of parameters are used to define bounds and targets for the 2D FDTD sweeps described in the next section. Note that this calculation just shows the nominal best grating period for each fill factor but does not show which combination of period and fill factor results in the highest overall coupling efficiency. Results from the 2D parameter sweeps should fit close to these two lines and indicate a preferred design.

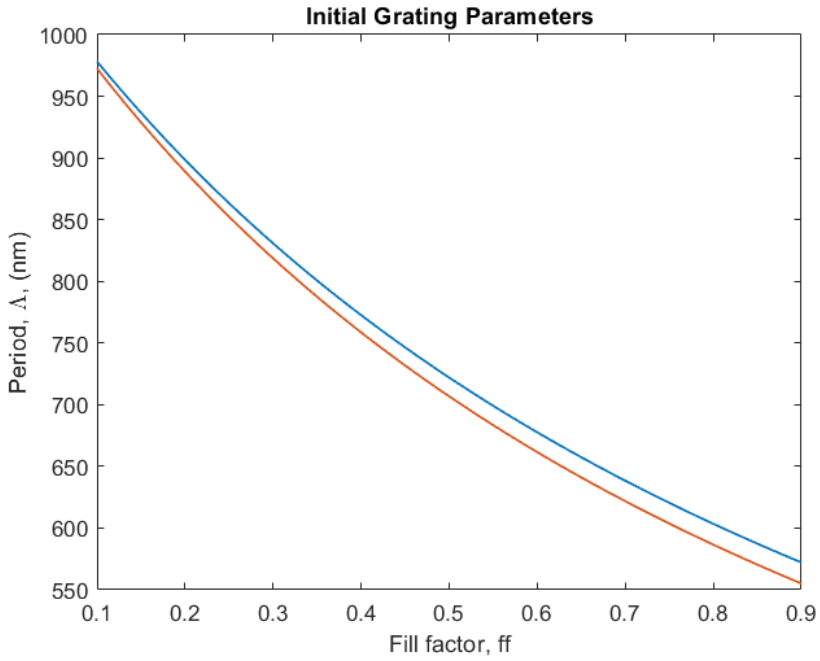

Figure 26: Combinations of period and fill factor likely to produce coupling according to the Bragg condition.

Collection Area Size

The size of each grating coupler collection area has a large impact on performance and affects fill factor, coupling efficiency, bandwidth, and tip/tilt behaviour. As the length of

the coupler and number of elements increases the strength of the diffraction behaviour also increases, narrowing and increasing the height of the transmission peak. At longer lengths the bidirectional nature of the grating coupler causes some input light to couple back to free space before reaching an output waveguide, which sets an upper limit on length. The overall coupling then tends towards zero with increasing length.

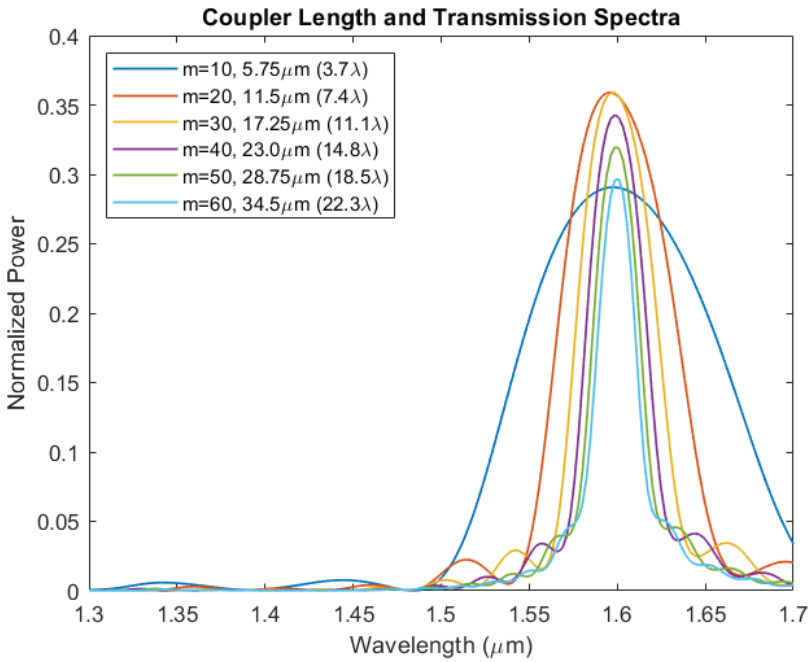

Figure 27: Transmission spectra for various coupler lengths. The peak narrows with increasing length.

If the target wavelength of the grating is chosen to be the peak power of the transmission spectrum, then the relationship between coupling efficiency and coupler size can easily be determined. Here a grating period and fill factor were chosen for operation at 1600 nm, and the number of elements was varied from ten to sixty. FDTD simulations show that the coupling efficiency is maximized for grating lengths between 10 μm and 20 μm. All fabricated four-arm grating couplers use collection area sizes within this range. Here the

bandwidth is defined as the FWHM of the peak and represents the wavelength range over which the grating coupler has high enough coupling efficiency to facilitate measurement.

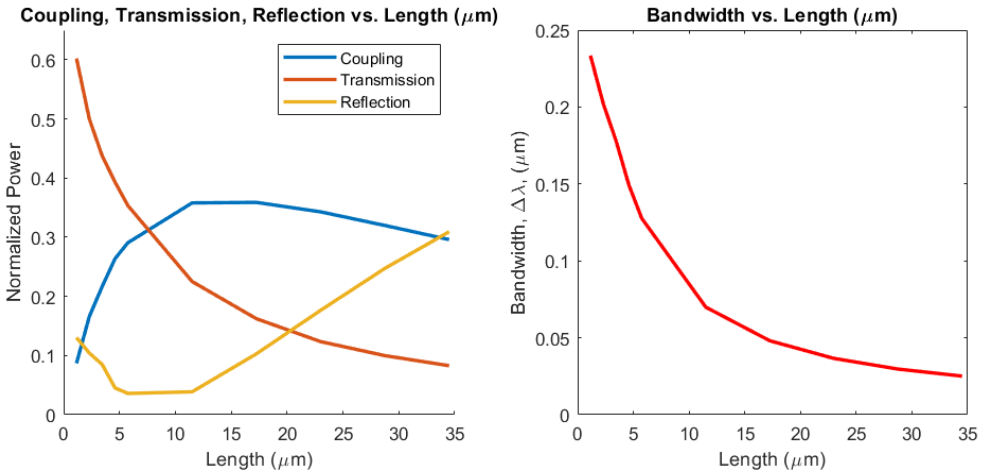

Figure 28: Coupling, transmission through the grating and reflection as a function of coupler length (left). Coupling spectral bandwidth as a function of coupler length (right).

It is assumed that a magnification system is used to downscale the wavefront to optimally fill the grating coupler array, meaning the absolute size of the array is not a factor in these calculations.

2D Parameter Sweeps

Parameter sweeps are performed in 2D using the OptiFDTD software package [75]. Both grating period and fill factor are swept over the ranges defined by the analysis above. The source for all simulations is a plane wave at 1550 nm situated above and centred on the structure. A BOX of 2 μm, TOX of 2.2 μm, and 200 nm Si device layer height are used to match fabrication process constraints. The response of the coupler is calculated using a monitor placed at the coupler's right-hand output. As such, coupling efficiency values only represent the output at one port, and the total coupling efficiency for these

simulations should be double due to symmetry. Vertical reflection and transmission are also monitored.

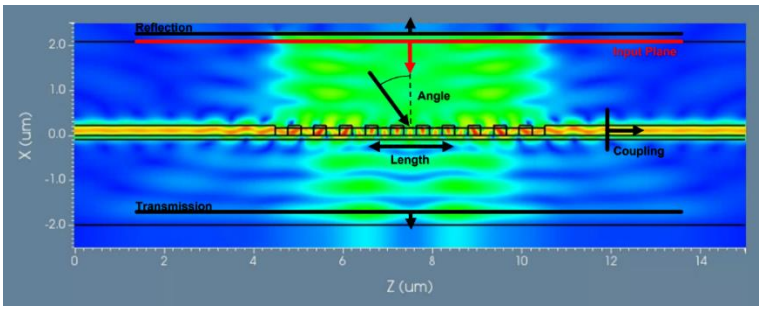

Figure 29: Visualization of 2D OptiFDTD simulations showing material structure, fields, sources, and monitors.

A coarse sweep was performed using periods from 400 nm to 850 nm and fill factors from 0.2 to 0.9. The results match theory well, with a band of good designs following the trend defined by the Bragg condition.

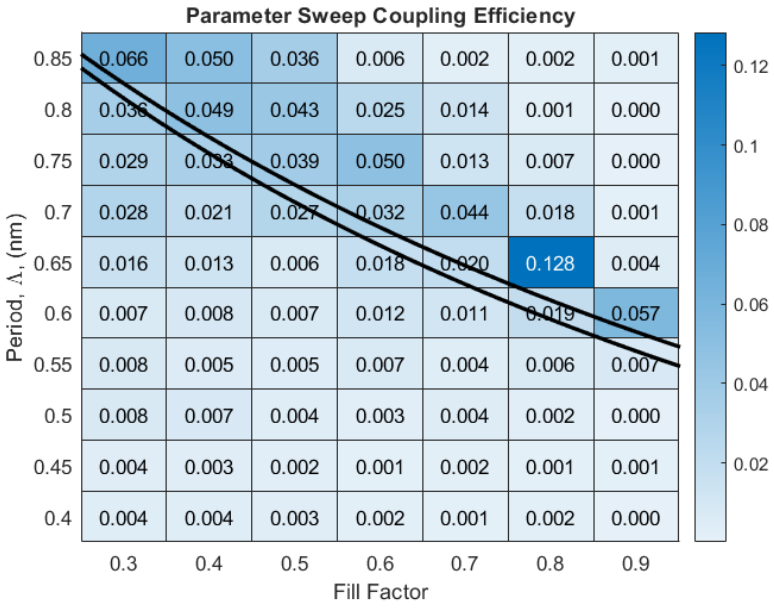

Figure 30: Simulated coupling efficiencies as a function of period and fill factor. Overlay is Bragg condition prediction.

There is a clear maximum at a period of 650 nm and fill factor of 0.8. Using these results as a guide a second finer scan was performed with periods from 625 nm to 675 nm and fill factors from 0.775 to 0.825.

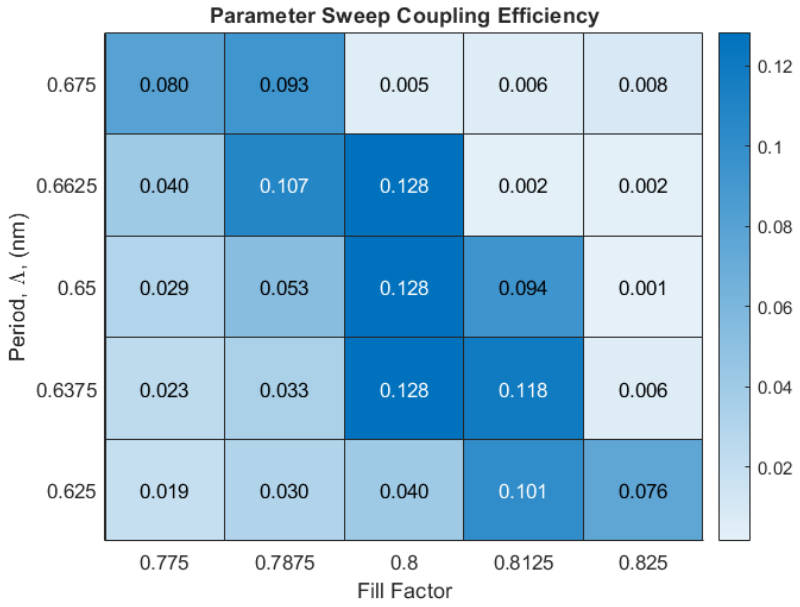

Figure 31: Coupling efficiency over smaller design space area of interest.

These results show the band of good designs in finer detail. The maximum coupling efficiency is 12.8% for a single output port. Though coupling efficiency is an important parameter, the real target is to produce a coupler with a monotonic relationship between incident angle and output power. This means the best design is not necessarily the coupler with the highest coupling efficiency, but rather the one that produces a relationship giving the best sensitivity and angular range for the target application. The output spectra of various designs were analyzed to select a final candidate design. A grating with a period of 639 nm and fill factor of 0.8 produced the spectrum shown in Figure 32, which has a high coupling peak offset from the target wavelength of 1550 nm

by about 30 nm. Though the coupling is not maximized due to the offset, the resulting relationship should be invertible as the angle-induced wavelength shift will increase measured power in one direction and decrease power in the other.

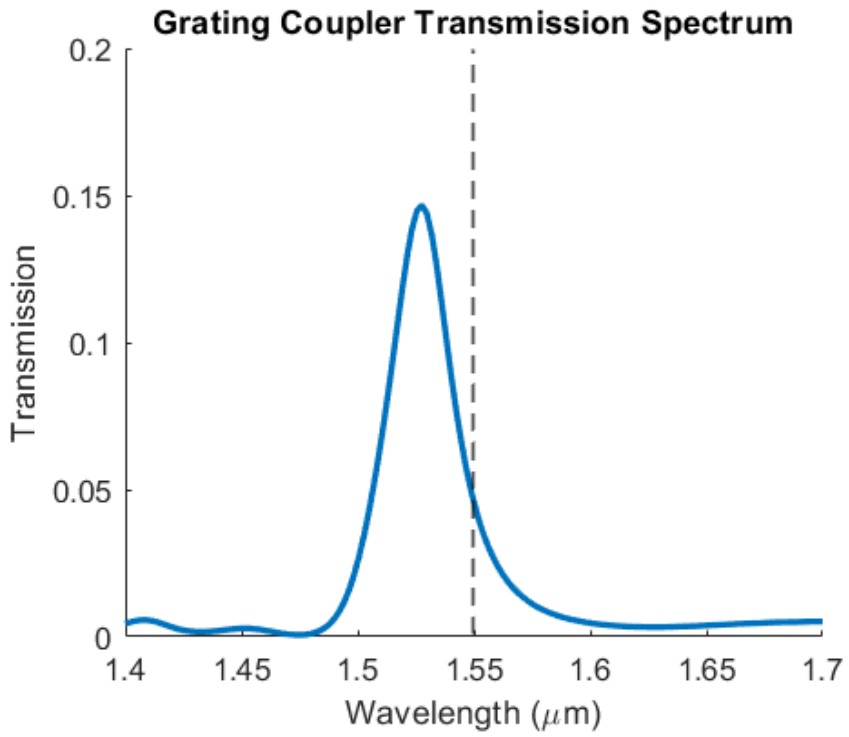

Figure 32: Grating coupler spectrum for the selected design at period = 639 nm and ff = 0.8.

The predicted angular response is analyzed by simulating over different input angles and plotting the output power at each. Note that in this case the height of the peak also changes with angle. The figure inset clearly shows an invertible relationship for operation at 1550 nm, though it is limited to ±3° and is not symmetrical nor fully linear over this range. This will not affect the device's ability to produce a unique solution.

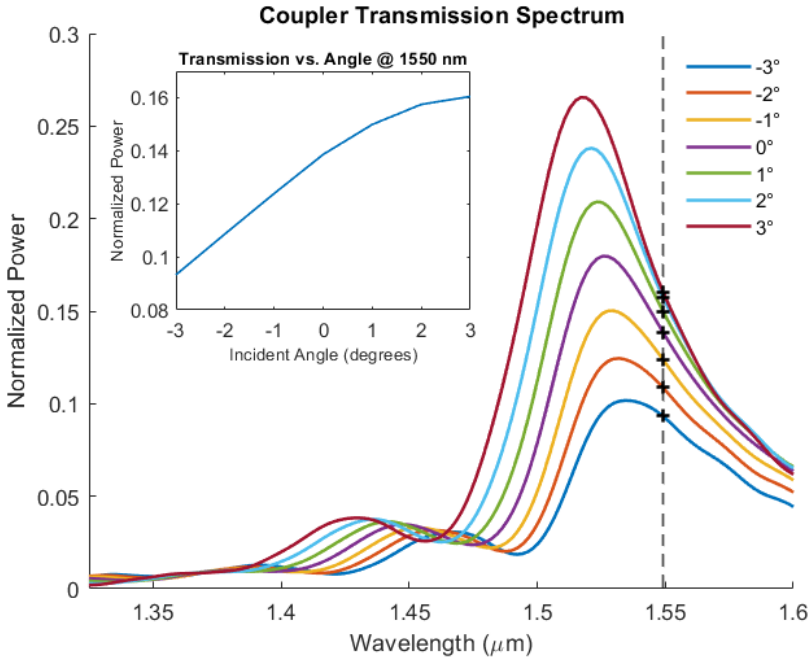

Figure 33: 2D simulation tilt behaviour of selected design showing a monotonic response (inset).

3D Verification

Nanophotonic devices designed using 2D simulations should be verified in 3D to quantify any errors introduced by the 2D approximation. The simulation geometry follows the same parameters as the 2D simulation, again matching fabrication process constraints. Only one of the four output arms is simulated to reduce computational requirements.

Interestingly the previous design does not perform as expected, with low coupling around 1550 nm. Further simulation of a preliminary grating coupler designed by fellow graduate student Ruslan Khabibrakhmanov reveals a design having more favourable characteristics with a period of 572 nm and fill factor of 0.82. This design is also simulated in 2D, where the coupling peak is lower and offset from 1550 nm. It is clear

that the assumption used to correlate 2D gratings and 3D nanohole array designs does not hold particularly well and results in a spectral shift of around 175 nm for these gratings and target wavelengths. Despite this, it is important to investigate both designs to quantify the utility of each design process. Both designs, one from 2D simulations and the other from 3D simulations, are included in the prototype for evaluation.

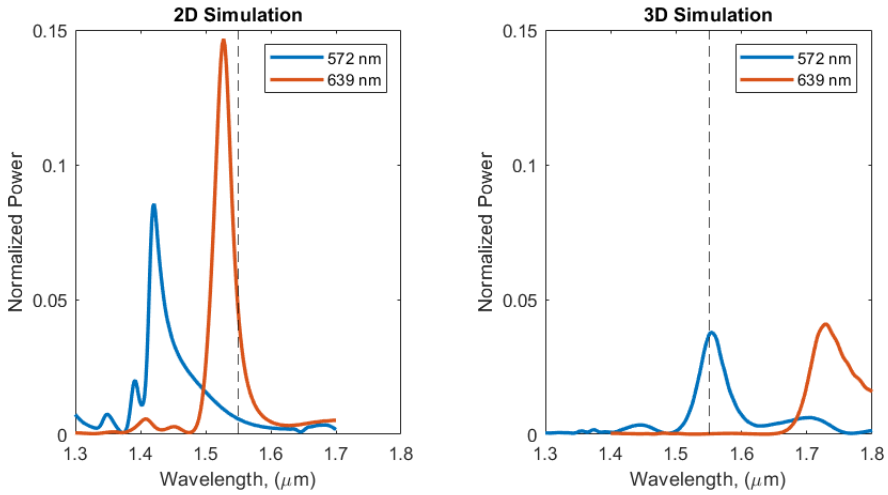

Figure 34: Coupling spectra of 572 nm and 639 nm nanohole gratings simulated in 2D (left) and 3D (right).

Optimization

The goal of designs thus far is to verify that four-arm grating couplers can measure local tilts. They have therefore been designed using the monotonic relationship between tilt and power as the figure of merit, without considering other factors such as compactness. Further optimization techniques can be used to increase coupling efficiency and reduce footprint, therefore improving overall grating coupler performance. Our optimization process targets two discrete domains. 3D simulations can optimize the geometry of the

grating collector area to improve coupling into the output grating mode. 2D simulations are then used to design improved tapers for coupling light from that grating output mode to a much smaller waveguide mode for routing on chip. The optimization in this work covers only the preliminary taper designs, and they have not yet been fabricated to verify their performance.

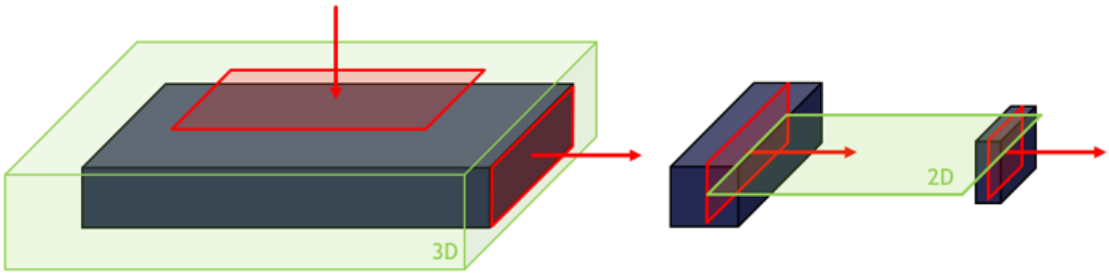

Figure 35: Optimization framework. Grating collection area is optimized in 3D while taper area is optimized in 3D.

It is important to maximize the fill factor of the arrayed collector to improve power collection efficiency and sampling of the incoming wavefront. This involves increasing the ratio of active coupling area to passive routing area. The main contribution to routing area for arrays with hundreds of inputs or fewer is waveguide tapers which convert diffracted light into an appropriate waveguide mode. Ideally these tapers are as small as possible without sacrificing performance. For the four-arm grating coupler application the target taper length is half the side length of the grating collector area, or 5 μm. For low loss one can use a linear adiabatic taper which utilizes a small convergence angle to gradually convert the large mode to the smaller one without coupling power to higher order radiating modes, however these are generally very long taking up valuable collector

area. A general guideline for adiabatic behaviour first proposed by Milton and Burns limits the local half-angle of the taper to

$$\theta < \frac{\lambda_0}{2Wn_{eff}} \tag{29}$$

where W is the local full width and n_{eff} is the effective index of the taper [76]. Recent simulation work done by Fu et al. shows this adiabatic limit can realistically be increased by a factor of 1.4. They showed that linear adiabatic tapers from 12 μm to 0.5 μm waveguide widths must be over 400 μm long and demonstrated a non-linear adiabatic taper that achieved > 98 % transmission with a length of 120 μm [77]. Even with this improved result the length is still at least an order of magnitude longer than desired.

To verify this result, linear tapers are simulated using 2D FDTD. The taper input is 10 μm and the output is 0.5 μm to match the required collector size and waveguide width. Taper lengths range from 5 μm to 40 μm to match target specifications, even though these will not necessarily result in adiabatic behaviour. A single mode at 1550 nm is injected into the input and the transmission spectrum is analyzed at the output.

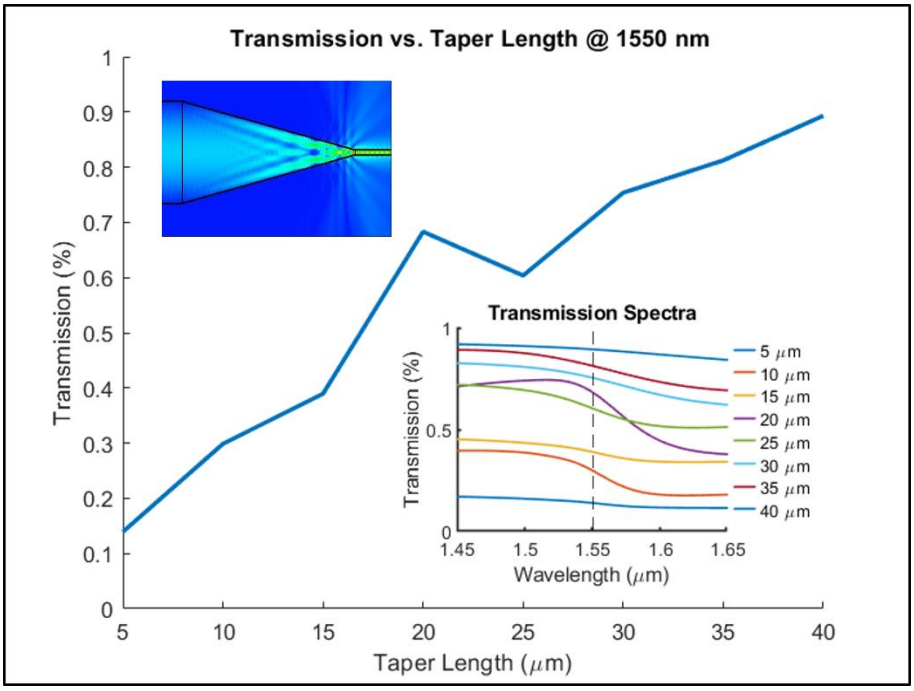

Figure 36: Transmission between fundamental modes before and after a linear taper. Image inset shows the clear presence of radiating modes.

The results are plotted in Figure 36 and show a clear increase in performance with taper length, as expected, from around 15% to almost 90%. The upper figure inset shows a top down view of the device geometry and the resulting fields clearly showing the presence of radiating modes which are the main source of loss into the surrounding cladding. While taper performance can approach 90%, the 40 μm taper length is still much longer than the target.

Topological optimization using the adjoint method is used to improve taper performance. The figure of merit is defined as the amount of coupling from the input waveguide mode to the output waveguide mode. The design is represented by a grid of pixels that have a refractive index between that of Si or SiO_2, where the initial pixel values are defined by the designer. For each iteration in the optimization process, a forward and adjoint

simulation calculate the gradient of the figure of merit with respect to each pixel in the design field. Each pixel then has its refractive index modified proportional to that gradient. The design can be improved by repeating this process. Binarization of the design field forces the values of the pixels to converge to either Si or SiO_2. A user-defined minimum feature size is enforced using a conical filter, which ensures the resulting designs will be fabricable.

Shown below is a taper design from a 5 μm waveguide to a 0.5 μm waveguide. The initial design is chosen to be a linear taper surrounded by a region with average refractive index. The length of the taper is set at 5 μm for comparison with the linear tapers simulated above.

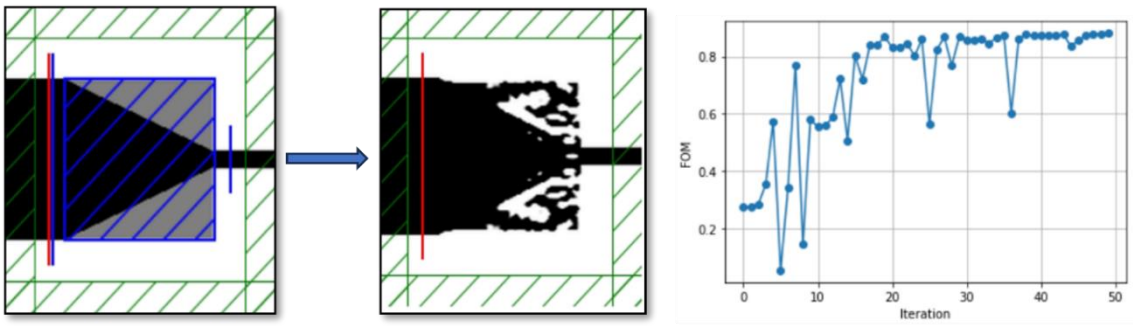

Figure 37: Progression of design from initial guess to final binarized and feature size limited design (left), trend of coupling efficiency vs. iteration number.

The results show a final coupling efficiency of around 90% after just 50 iterations, much improved over the 15% efficiency seen with the linear taper. The final design obeys minimum feature size constraints and is completely binarized.

Chip Layout

The last step in the design process is to assemble all candidate four-arm coupler designs into a single chip that facilitates testing. The final submitted fabrication schematic is created using KLayout and is shown below [78].

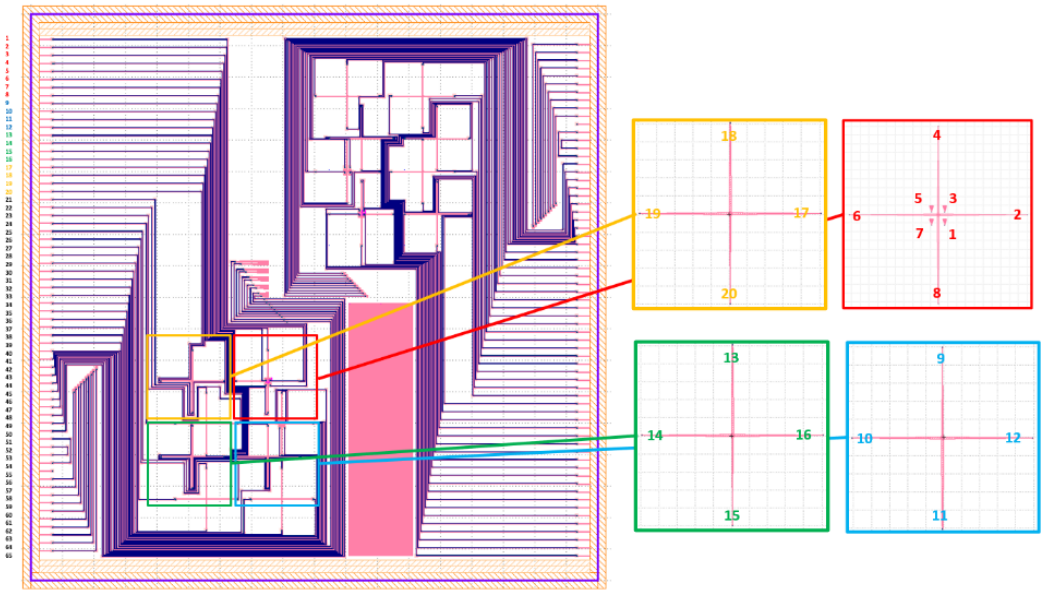

Figure 38: Chip schematic as designed in KLayout. The highlighted areas show the locations of four-arm grating couplers.

Each nanohole device is created using a custom python script using the gdspy package [79]. The script builds each grating from a series of individual polygons defined by the design period and fill factor and writes them to a GDSII file. These files can then be imported into KLayout to create the final master schematic. An example four arm device is shown in Figure 39.

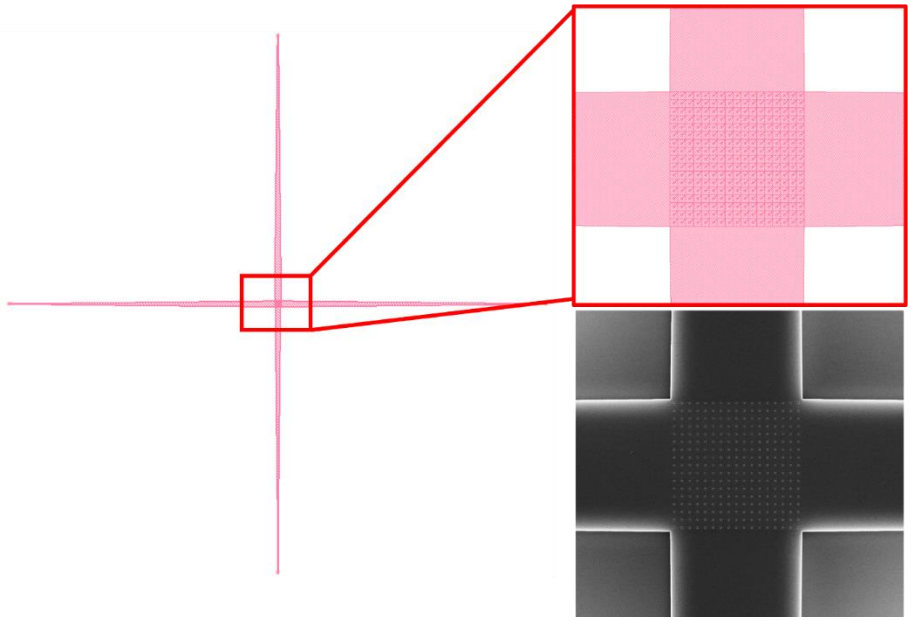

Figure 39: A four-arm grating coupler including waveguide tapers as seen in KLayout (left). The image at the bottom right is taken by SEM after fabrication.

Device outputs are routed to edge couplers on the left and right edges of the chip to allow fiber coupling or measurement via a camera. Each of the four arms is routed to adjacent outputs spaced at 127 μm so that a single fiber assembly can be used to measure all outputs from a single coupler simultaneously. The other two edges of the chip provide a space to physically manipulate the chip with tweezers. Standard grating coupler components are placed surrounding the four-arm structures to assist with alignment. These should have very high coupling efficiency and provide a reference for the position of the input light. A set of four edge couplers facilitates alignment of an edge coupled fiber assembly. A set of ten grating couplers with varying taper lengths provides a baseline for measuring taper performance as a function of length. In all cases, care is taken to ensure edge coupler outputs are not in line with the four-arm structures on the surface of the chip to reduce the effect of reflections on measurements.

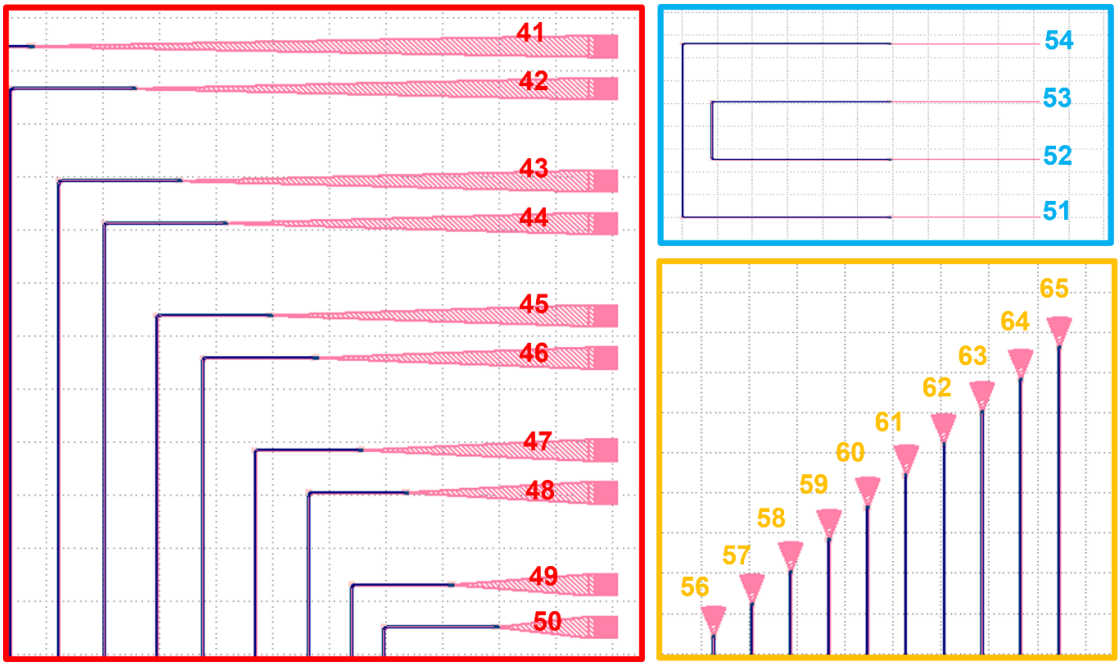

Figure 40: Taper length test structures (red), alignment edge couplers (blue), vertical edge couplers (yellow).

Two chips have been fabricated, each described here for reference. For each, output ports are numbered starting from the top of the chip's left side as viewed as a GDSII file in KLayout and continuing counterclockwise. The first chip was designed by fellow graduate student Ruslan Khabibrakhmanov and contains only 572 nm and 584 nm four-arm gratings, as well as some other structures not relevant to this work. The second chip contains 572 nm, 584 nm, and 639 nm four-arm gratings as well as alignment couplers and the taper length structures described above.

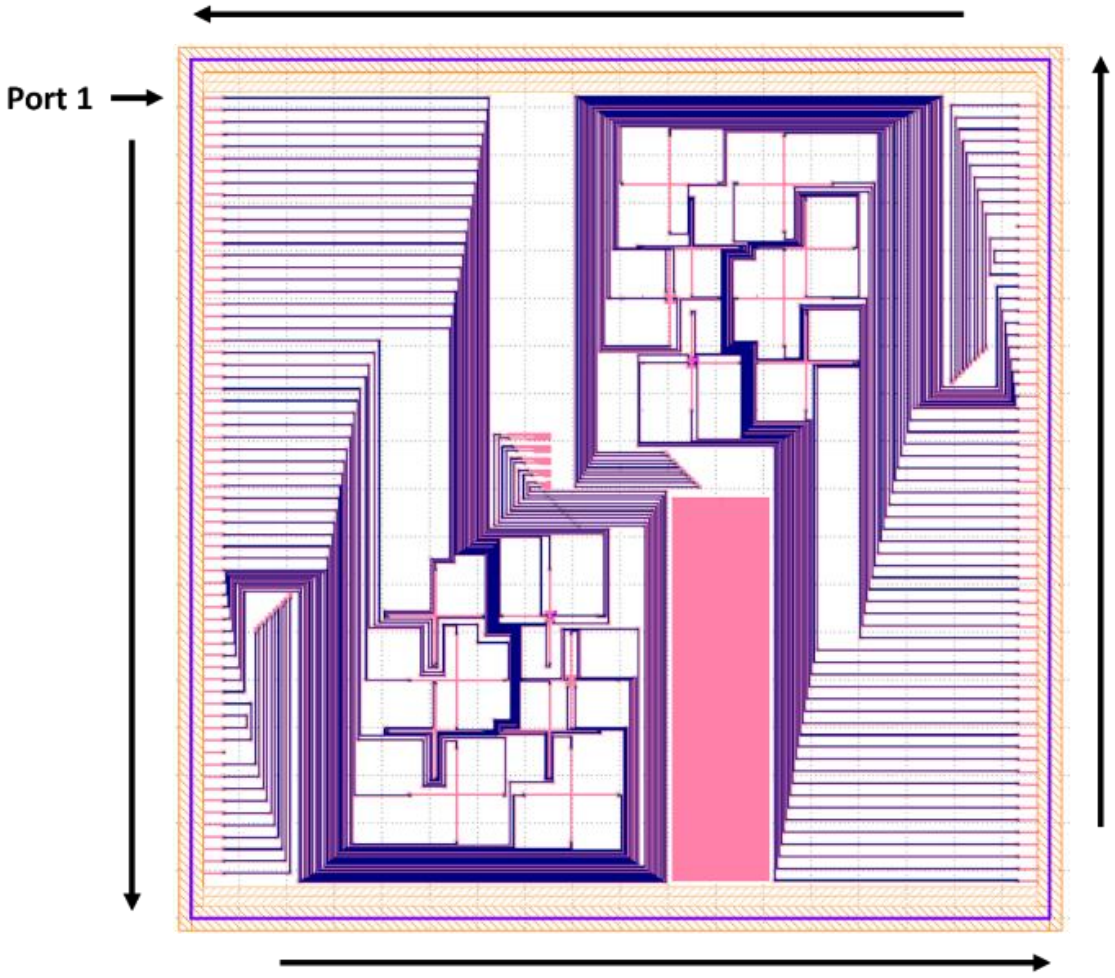

Figure 41: Definition of port numbers, starting as indicated and increasing counterclockwise.

Note that for both chips the origin is defined as the centre of the chip, more specifically the rectangular box placed on the "Chip Floor Plan" layer. Structure locations in the table below reference this origin.

Table 2: Device definitions of the two fabricated chips.

Chip	Device Name	X pos (µm)	Y pos (µm)	Ports
748 - Wavefront Sensors (Ruslan Khabibrakhmanov)	Four-Arm Grating (572 nm)	-3350	1650	13 - 16
		-2070	-145	17 - 20
		-3350	-145	21 - 24
	Four-Arm Grating (584 nm)	-2070	-1910	25 - 28
		-3350	-1910	29 - 32
		-3350	-3240	33 - 36
1211 - IPJMMAP1 (Alexander Parent)	Four-Arm Grating (639 nm)	-745	-1330	2, 4, 6, 8
		-745	-2530	9 - 12
		-1945	-2530	13 - 16
		-1945	-1330	17 - 20
		-1715	-2000	21 - 24
		-1715	-3200	25 - 28
		-515	-3200	29 - 32
		-515	-2000	34, 36, 38, 40
	Taper Length Testing	-750	300	41 - 50
	Four-Arm Grating (584 nm)	745	1330	67, 69, 71, 73
		745	2530	74 - 77
		1945	2530	78 - 81
		1945	1330	82 - 85
	Four-Arm Grating (572 nm)	1715	2000	86 - 89
		1715	3200	90 - 93
		515	3200	94 - 97
		515	2000	99, 101, 103, 105

Test Setup

Once fabricated, chips are evaluated using a custom automated test setup to verify the predicted monotonic relationship between output power and incident angle for each of the fabricated four-arm grating coupler structures. This requires a 1550 nm coherent light source with tunable incident angle and polarization control, as well as relative power measurement between each of the four outputs. A diagram of the system along with major components is in Figure 42.

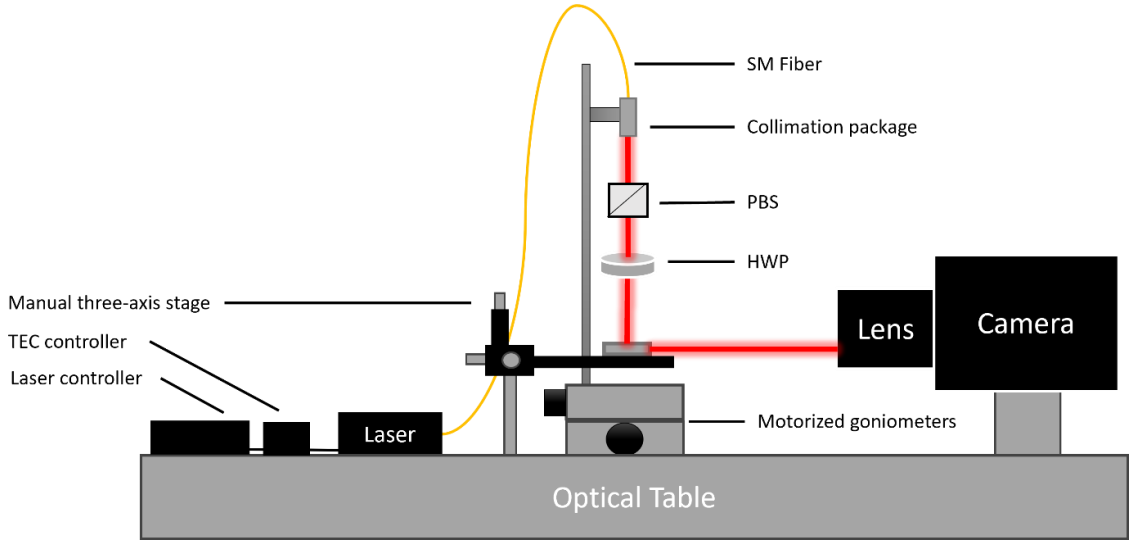

Figure 42: Experimental test setup.

Hardware

Light is provided by a 1550 nm Fabry-Perot laser from Thorlabs outputting 100 mW of optical power. This light is routed via single mode optical fiber to a collimation package mounted on a programmable dual-axis goniometer stage assembly from Newport. The collimated beam then passes through a polarization beam splitter (PBS) which ensures linear polarization and a half wave plate (HWP) which gives polarization state control. From here the light strikes the surface of the chip, illuminating the device under test (DUT). The spot size is much larger than the collection area of each device in this study, making the incident beam essentially a plane wave. A focusing lens may be inserted into the optical path between the HWP and the chip to reduce the beam spot size and increase the intensity at the DUT.

Table 3: Part numbers of test components.

Device	Supplier	Part Number
Fabry-Perot Laser, Pigtailed Butterfly Package (1550 nm)	Thorlabs	FPL1009S
Motorized Goniometer, ±45°, Micro-step Drive	Newport	BGS80PP
Motorized Goniometer, ±45°, Micro-step Drive	Newport	BGM120PP
IR Camera	Xenics	XEN-000112

The chip is mounted on a manual three-axis translational stage to allow for precise positioning. The vertical position of the chip must be such that the top surface is exactly aligned with the rotational axes of the goniometers to ensure there is no translation of the spot across the chip at large incident angles. This is done by raising the chip to the height specified as the centre of rotation of the goniometer stages. The beam must pass through this centre of rotation as well. Each DUT is selected by aligning it to the beam by moving the chip in the plane parallel to the optical table. Good alignment can be verified by ensuring the point of reflection of the beam off of the top surface of the chip does not change position even at the extreme ends of the angular scan range.

Light from each DUT is routed to an edge coupler where it is emitted towards a magnification system and infrared camera from Xenics. Both the magnification system and camera can be precisely positioned to adjust focus and zoom. The laser current, camera gain and integration time are tuned to provide good contrast between the output port areas of the image and the background pixels. It is also important to ensure none of the pixels in the measurement regions are saturated, as this would artificially reduce the measured power.

Software

Scanning is performed by an application developed in C++ and MATLAB. Motor control is performed by compiled MATLAB executables written by undergraduate student Archie Dubey which allow certain functions like finding the home position at vertical incidence or stepping a specified number of degrees in either angle to be called at any time. This is particularly useful in aligning the laser to the desired DUT. The main scanning application handles communication to the camera and motor controller modules, executes the angle scan by stepping through user defined motor positions and taking an image at each, and saves all images to a local location. The images are then post-processed in MATLAB to define areas of interest and compute relative power by integrating pixel values. The combination of MATLAB and C++ code gave the greatest flexibility allowing each module of the system to be operated both standalone and as a system. Scan parameters including angle range, angle resolution, and camera integration time can be set using a single text file. Camera integration time and laser power are tuned before each scan by viewing the output and making manual adjustments. It is critical to limit the effects of low power, pixel saturations and top surface reflections on the output areas.

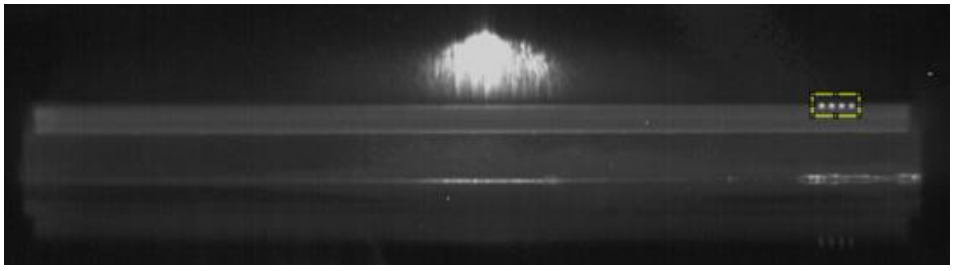

Figure 43: A typical image taken by the IR camera.

The image processing script is developed in MATLAB and leverages functionality of the Image Processing Toolbox [80]. The script allows the user to graphically define areas of interest directly on an image, removing areas with artifacts due to reflections from the chip. Routines then search this area of interest for output ports using a built-in contour finding algorithm and sum pixel values to calculate the relative power in each port. This is shown in Figure 44. The locations and sizes of the output ports may also be set manually for cases where none of the test images have light on all outputs simultaneously, as in these cases the algorithm cannot find the locations of all the relevant ports. The user must define which of the outputs corresponds to each of the four UP, DOWN, LEFT, and RIGHT arms, something easily done by referencing the chip layout. The set of incident angles used for each image is encoded into the image filenames which are extracted by the script. From here the relationships between power and angle can be analyzed using Equations (24) and (25). Polarization scans are performed by manually rotating the HWP through all polarization states of interest and taking an image at each one. Images are analyzed in a similar manner using Equation (26).

Figure 44: Automatic output port detection using a MATLAB script.

Results

Design performance is verified in two ways. FDTD and FEM simulations are used to predict coupling efficiency and tilt response over different incident angles and polarizations. Prototype device measurements provide further design verification. This is especially relevant due to the discrepancy between 2D and 3D simulations. Incident angle and polarization are varied over the same ranges defined in the simulation results to provide a comparison.

Simulations

572 nm Four-arm Gratings

Simulations for the 572 nm four-arm gratings were done by fellow graduate student Aydin Amini using the FEM solver COMSOL. The analysis was performed in 3D at 1550 nm over varying incident angles and polarization states. Here the incident angle is defined by a polar angle, θ, and azimuth angle, ϕ, while polarization is denoted ϕ_0. The incident angle is kept within 2° of vertical, and polarization is scanned across all possible values. Monitors are placed at each of the output ports to calculate the coupling efficiency into each one. The output of the simulation is four sets of four-dimensional data, one for each output port. Analyzing these using the monotonic relations allows tilt response to be estimated.

In order to compare simulated and measured results the θ, ϕ basis must be converted to the α, β basis used by the test setup and monotonic relations. Here α and β are rotations

of a vertical unit vector about the x and y axes, respectively. This formulation holds for small values of α and β.

$$\alpha = \arctan\left(\frac{\sin\theta\sin\phi}{\cos\theta}\right) = \arctan(\tan\theta\sin\phi) \tag{30}$$

$$\beta = \arctan\left(\frac{\sin\theta\cos\phi}{\cos\theta}\right) = \arctan(\tan\theta\cos\phi) \tag{31}$$

For most polarization states, results for the 572 nm gratings show a linear and clearly monotonic relationship for both α and β as expected. This ideal behaviour is seen at polarization states around 45°. For polarizations near 0° or 90° the coupling into two of the output arms goes to zero depending on alignment, making the monotonic relations not well defined. In these cases, the 572 nm design would only be able to determine one of the incident angles. It is therefore important to align the input polarization to 45° to ensure the best operation. The data for each spatial angle (α, β) is plotted for all values of the other spatial angle and shows that these two relations are independent of one another. The trends have a good linear fit over the simulated angles.

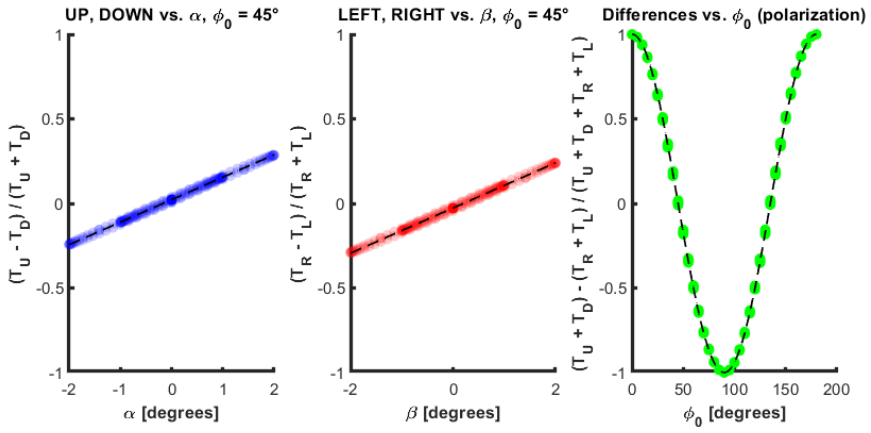

Figure 45: Simulated results of monotonic relations as a function of each of the three angles for the 572 nm design.

The polarization response is sinusoidal, which also matches expectations. It exhibits a twofold degeneracy for any two polarization states symmetrical about either the vertical or horizontal axes of the grating, which is expected since the magnitudes of the x and y polarization components are identical in these cases, the only difference being the relative phase difference.

639 nm Four-arm Gratings

Simulations for the 639 nm grating couplers were done in 3D using OptiFDTD and the same input scan parameters. As predicted by the 3D design simulations, this design of coupler has low coupling efficiency at 1550 nm. Since the coupling peak is significantly offset from 1550 nm, a monotonic relationship cannot be expected at this wavelength.

Measurements

Uncertainty

Experimental measurements are meaningless without some quantification of the uncertainties involved. Statistical uncertainty in the following measurements arises due to fluctuations in laser power and camera pixel sensitivity. It is calculated by taking repeated measurements of output power from a four-arm grating at a single input angle and performing a Gaussian fit to the resulting monotonic relation values. Individual output ports are not analyzed separately as the sources of error are correlated across entire images, affecting each port in the same way. The monotonic relations for both α and β are similar, with contributions from only two output ports. The statistical uncertainty for these calculations is therefore taken to be the average between the two. The relation for

ϕ_0 involves contributions from all four output ports and is given a separate value. All images are taken with the laser power and camera integration time set to those values used in measurement, with angles set to $\alpha = 2°$, $\beta = 2.5°$.

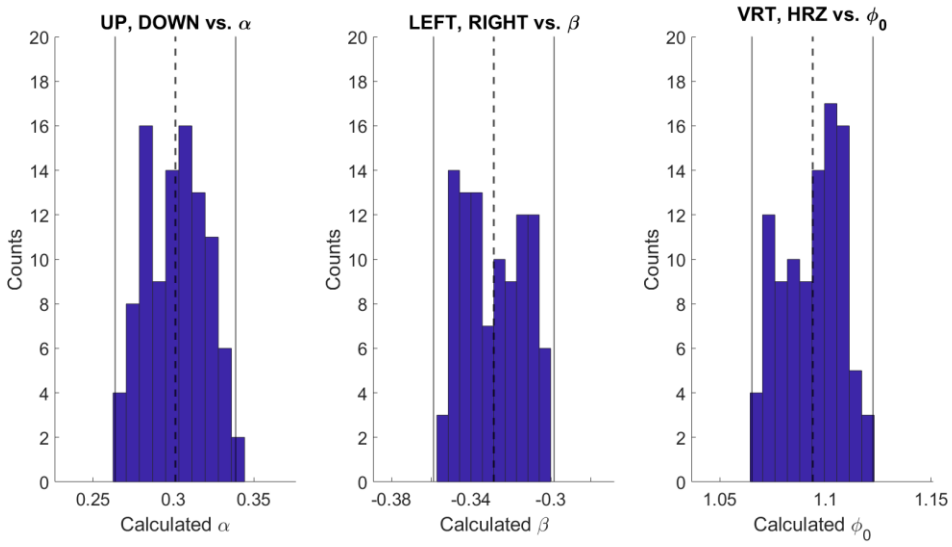

Figure 46: Distributions of calculated monotonic relations.

The resulting 2σ uncertainty values are 0.034 for α and β, and 0.029 for ϕ_0.

572 nm Four-arm Gratings

The 572 nm structures have good coupling efficiency at 1550 nm and are therefore easily visible in the test setup camera. High contrast was obtained without saturating the detector at a laser current of 250 mA and short integration time of 1000 µs. Incident angle was scanned over ±2° for comparison with simulated results. Polarization was set at 45° as this is the preferred operating condition for these grating couplers. The results show a strong linear correlation between incident angle and coupler output, as predicted by theory.

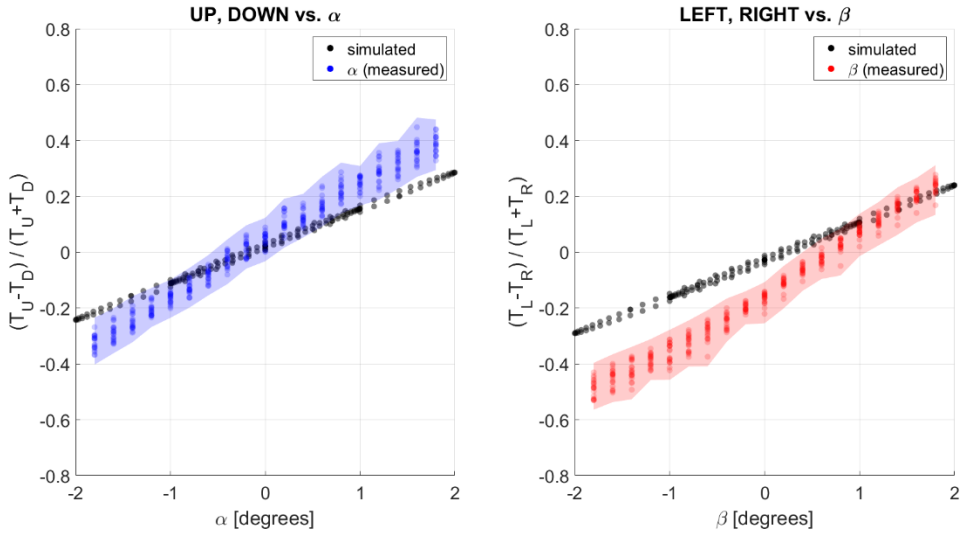

Figure 47: Measured spatial angle results of the 572 nm devices showing good agreement with simulated results. The monotonic relationship is well-defined and linear over the ±2° angle range.

There is no clear trend between each monotonic relation and the other spatial angle, showing that each is independent of the other. This is easily seen in Figure 48.

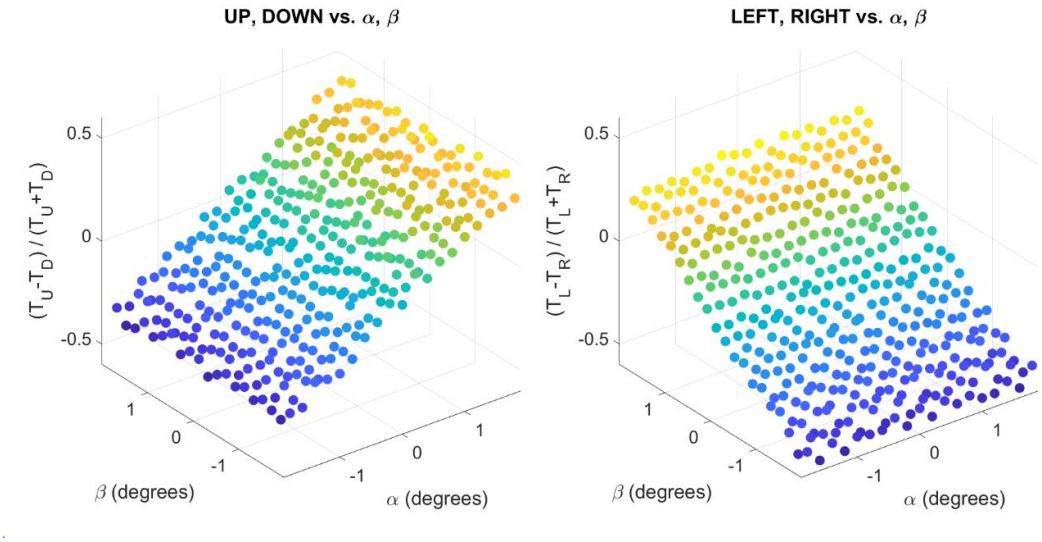

Figure 48: Measured monotonic relations vs. both spatial angles. The relation for α is independent of β, and vice versa.

Polarization scans at normal incidence confirm the expected sinusoidal relationship. Overall, these measurement results track well with the simulated predictions, confirming the theory.

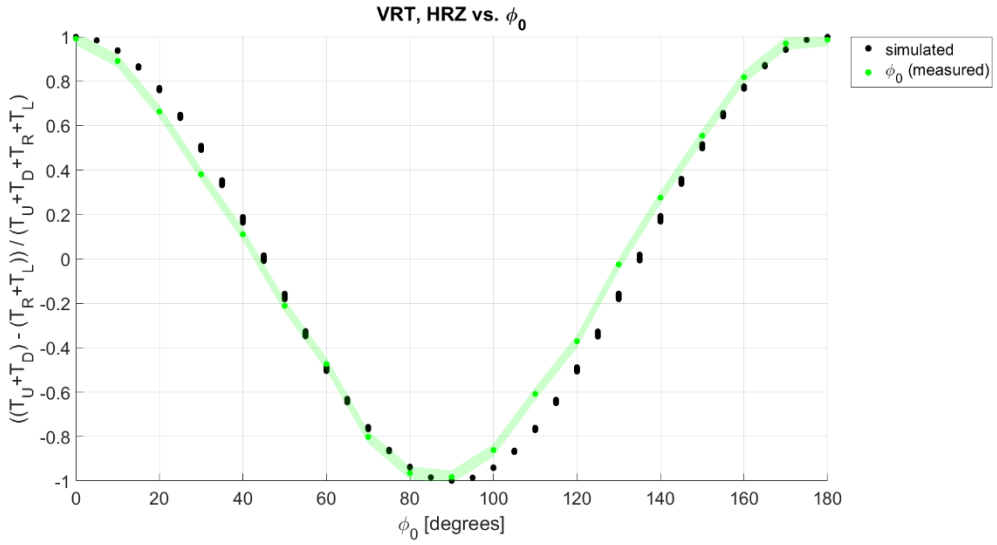

Figure 49: Measured polarization results of the 572 nm devices. There is a sinusoidal relationship as expected.

639 nm Four-arm Gratings

Measurements of the 639 nm gratings presented some challenges. The coupling efficiency of these designs is quite low at 1550 nm as predicted by the 3D design simulations. As a result, it is difficult to tune source and imaging parameters to obtain contrast suitable for measurement conditions. The simulation results also predict a limited change in output power for each incident angle, making it hard to discern any meaningful relationship between power and angle for these test conditions.

Discussion

It is clear from both simulated and measured results that the 572 nm four-arm grating coupler designs enable tilt measurement on a silicon photonic chip. Their measured performance closely matches simulations which validates both the 3D design and fabrication processes. For best performance the input polarization should be held at ±45°. The 639 nm gratings did not perform to their design specifications. It is clear that the 2D approximation used here is not sufficient to represent the behaviour of a 2D nanohole array, as the simulated results show a large shift in peak coupling wavelength. This is likely because the nanohole array operates in the subwavelength regime, where the effective index can be more accurately modelled using effective medium theory. This has been used successfully in other nanohole grating design works [81]. This was not used in the current design process but should be considered going forward.

The relationship between angle and power for these couplers appears linear over the tested angles, though it need not be so. In practice, one could calibrate a device by performing an angular sweep of a single grating coupler to extract the coefficients of this linear relationship, then perform a fitting to convert from measured power in the four output arms to α and β. If a similar grating coupler designed for a different target application but using the same operating principles were to have a nonlinear relationship, either a polynomial fit or lookup table would also facilitate this conversion. The

preferred approach would be determined by the control electronics and be a trade-off between accuracy and speed.

There is a discrepancy between the measured and simulated results in the form of a small shift in both the slope and offset of the linear relationship. The slope shift could be due to a shift in the coupling spectrum as a result of fabrication tolerances. According to Chrostowski and Hochberg, the centre wavelength of a grating coupler may deviate from the FDTD design target by up to 10 nm, something which has been shown to affect the monotonic relationship [72]. Another likely contribution is the presence of systematic error in the test setup due to angular misalignment, which could account for the linear offset. The monotonic relations for each of the spatial angles should pass though the origin of Figure 47, and have a value of zero at normal incidence. Under this assumption the angular offset is approximately -0.25° for α and 0.75° for β. It is feasible that angular misalignment of this magnitude is present.

Simulations and measurements only guarantee tip/tilt performance up to ±2° from vertical, which is sufficient for wavefront sensing applications. It is likely that larger angles would eventually shift the coupling peak too far from the target wavelength, resulting in a loss of performance. As seen from the collection area size study, the coupling peak can be made wider by reducing the size of the coupler. This would likely increase the useable angular range but decrease the overall coupling efficiency and reduce the angular sensitivity. Grating coupler size is therefore a design variable to consider when targeting specific applications.

The performance of these devices as wavefront sensors can be compared to other approaches. The bandwidth of the four-arm grating coupler array wavefront sensor is fundamentally limited by photodetector bandwidth which can reach 265 GHz in a Ge-based design, much higher than the speed of CMOS arrayed detectors [82]. In practice however, the speed of the reconstruction algorithm dominates. The SHWFS requires a permanent mapping between each lenslet and its detector area which imposes a fundamental limit on optical dynamic range. Algorithmic variants such as sequential sampling can increase this range, but at the cost of system complexity and speed [83]. The four-arm couplers will work for any wavefront whose local distortion does not exceed the angle range of each coupler, ±2° in this case but also a design variable. One major benefit of the four-arm design is its implementation on a small chip which takes up far less space and weighs far less than the bulk optics used in a SHWFS. Other novel wavefront sensing approaches have been demonstrated including photonic lanterns, which consist of multimode to multi-core optical fiber tapers that provide spatial sampling of the wavefront. The phase information is encoded into the intensity of each of the single mode outputs, analogous to our approach. Calculating the relationship between phase and intensity is nonlinear, and requires the use of a neural network [84]. Janz et al. have demonstrated a silicon photonic solution consisting of closely spaced opposing grating coupler pairs that can measure local tilt in a similar way to a four-arm grating. Here the local wavefront tilt is proportional to both the power ratio between the two couplers as well as the relative phase between the two, which can be measured using a waveguide interferometer [85]. This approach has many of the same advantages and disadvantages

as the four-arm approach in terms of speed, size and complexity, but is limited in that each “pixel” consists of four individual couplers, which takes up valuable space and assumes the phase of the wavefront is correlated across all four couplers.

Silicon photonics as a platform outperforms AO in terms of operational bandwidth. The complex two-stage AO system used in the LCRD test reached a bandwidth of 20 kHz, while carrier-depletion phase shifters and photodetectors can operate in the gigahertz regime [37]. This is a clear advantage in extending to applications associated with stronger turbulence and requiring higher Greenwood frequencies.

Wavefront sensors have applications other than atmospheric turbulence mitigation including ophthalmology and microscopy which could benefit from a single chip silicon photonic solution. Wavefront measuring devices including SHWFS and AO have been used to quantify high-order aberrations in the human eye which normally cannot be corrected with corrective lenses alone. These aberrations affect even those with 20/20 vision, especially during low light conditions where the pupil dilates increasing the collection of off-axis light [86]. Adaptive optics also allows for increased resolution when imaging the cellular structure of the retina, a huge benefit in research and diagnosis [87]. Pyramid wavefront sensors have also been demonstrated in this field [88]. Wavefront sensing and AO have similar benefits in microscopy where they correct aberrations and increase the intensity of the collected signal [89]. Indirect wavefront sensing, also known as the sensorless approach, corrects a wavefront by maximizing resolution or intensity algorithmically over many consecutive measurements [90].

Though common in microscopy applications, this approach is slower than direct wavefront sensing and may not be suitable for communications applications.

Fabrication Errors

Scanning electron microscopy (SEM) images of various structures are used to verify the quality of the fabrication process. The goal is to validate the correlation between simulations and measurements and to provide guidance for future designs. Areas of interest include four-arm gratings, alignment couplers, and minimum feature size test structures. No fabrication errors are visible on the imaged four-arm grating couplers. The alignment couplers show under-etching in some regions, resulting in the joining of two or more adjacent grating lines. However, it should be noted that these designs have grating spacings of just under 70 nm and were known to violate minimum feature size constraints by a small margin. The test structures consist of arrays of nanoholes of varying radii from 100 nm to 240 nm. The 100 nm holes are occasionally not etched at all, with a yield of around 50%. When present, these holes may also be misshapen and clearly of the wrong size. The 120 nm holes show some inhomogeneities in uniformity, with some holes more elliptical than others. There is also a visible variation in size. No other hole sizes show any fabrication errors over the imaged areas.

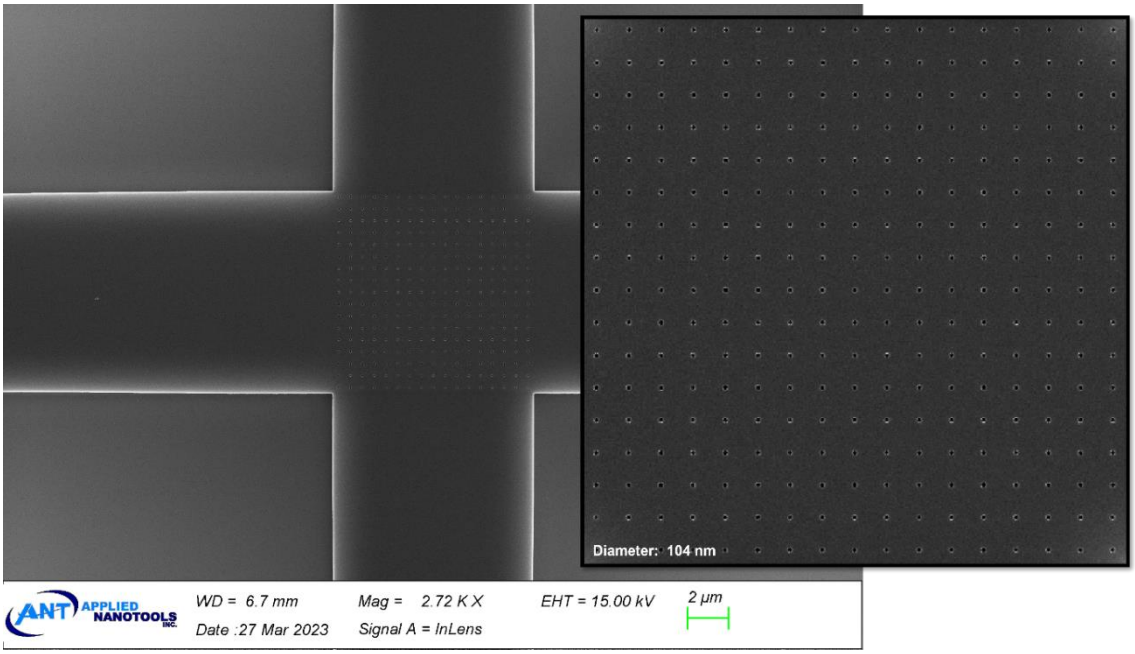

Figure 50: SEM images of 104 nm diameter nanoholes.

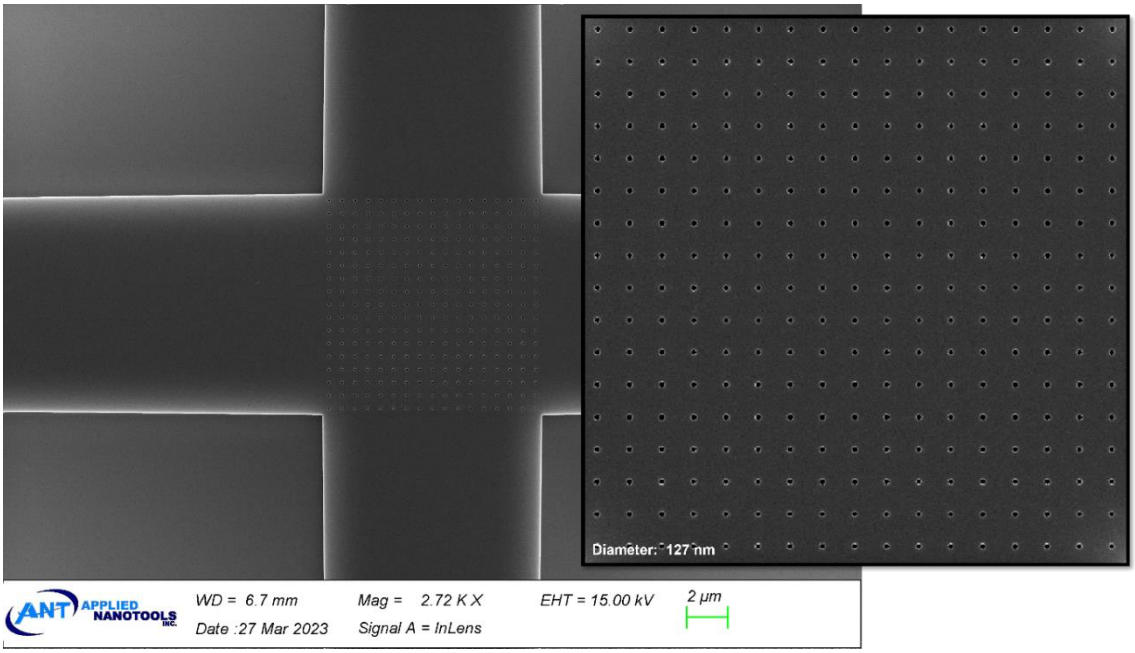

Figure 51: SEM images of 127 nm diameter nanoholes.

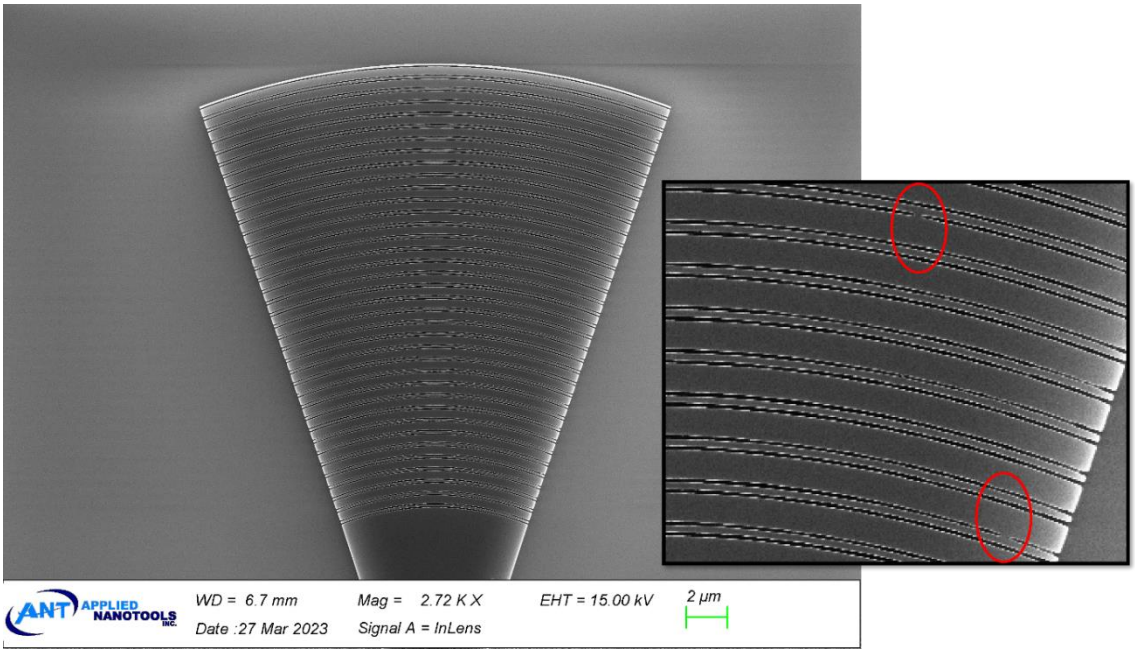

Figure 52: SEM images of alignment couplers showing the joining of adjacent grating lines.

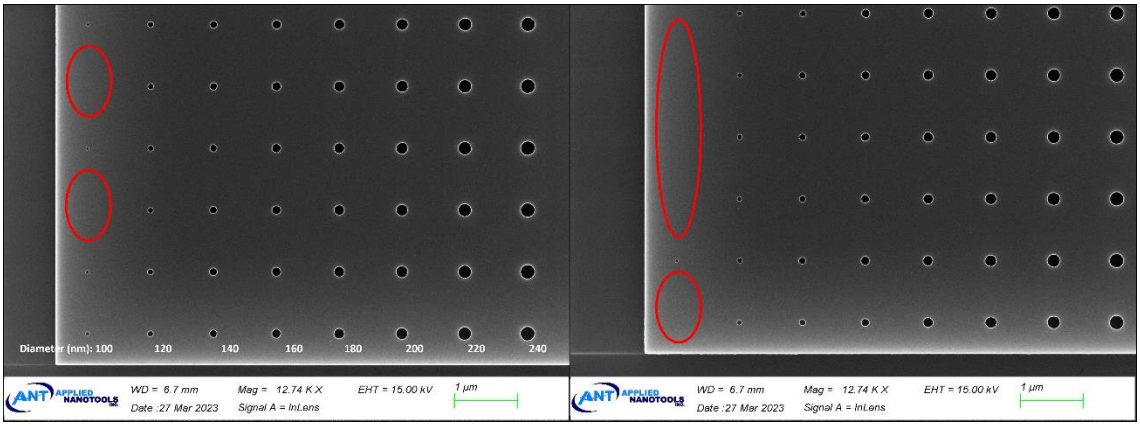

Figure 53: SEM images showing the absence of nanoholes.

These results motivate further restrictions on future designs. For gratings with approximately 50% duty cycle such as the alignment couplers, a minimum feature size of 80 nm is recommended. For more sparsely etched features such as nanoholes, a

minimum size of 140 nm is recommended. All future designs will benefit from being designed with fabrication tolerances in mind.

Future Work

This current work has successfully demonstrated tip, tilt and polarization measurement using a single four-arm grating coupler on a silicon photonic platform, acting as a proof of concept for an integrated silicon photonic wavefront sensing device based on an array of four-arm grating couplers. Future work will progress towards a fully functional wavefront sensor on chip. An important step is testing the current prototypes with a tunable laser to analyze their spectral response and correlate them with simulated results. It is not currently possible to measure the tip/tilt response of the 639 nm nanohole structures with the current setup as they have extremely low coupling at the 1550 nm laser wavelength. Correlating measured and simulated results will also help define a better relationship between 2D FDTD simulations and 3D nanohole structures leading to more accurate and efficient design procedures. As we have seen, the assumptions used to correlate 2D and 3D designs result in a wavelength shift. Further optimization of the collector area will result in increased coupling efficiency and tuning of monotonic relationships. We have already demonstrated here the power of techniques like topology optimization in taper design which can be extended to the entirety of the grating coupler. This will increase both the dynamic range and sensitivity of a completed wavefront sensing device. Taper designs should be verified with fabrication and measurement. Though topology optimization can result in very high figures of merit in the simulation domain, it is important to analyze the effect fabrication tolerances have on small features.

Once an optimized grating coupler element is achieved with sufficient coupling efficiency and compactness it should be tiled in an array to demonstrate local tip/tilt measurement and phase estimation at the device level. An example device schematic is shown in Figure 54.

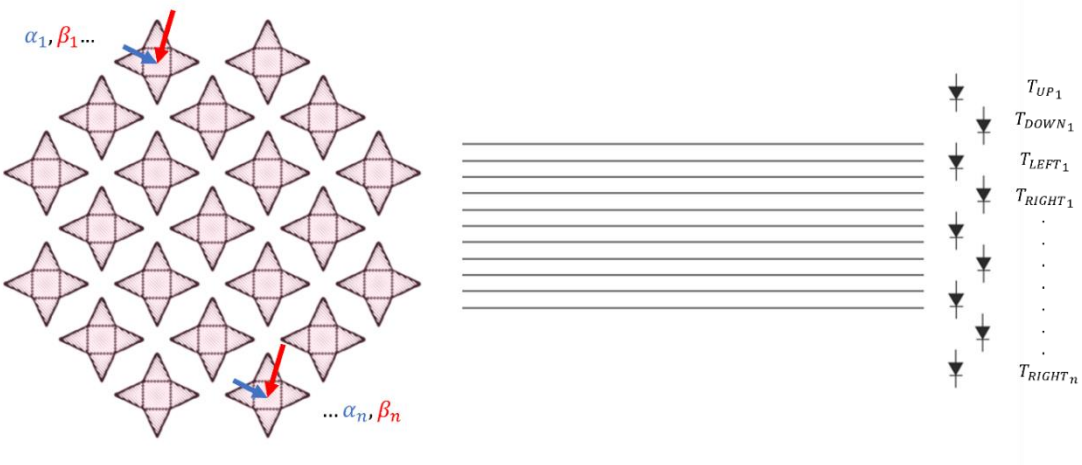

Figure 54: Schematic of an arrayed four-arm grating wavefront sensor.

Conclusion

We have successfully demonstrated a four-arm grating coupler capable of measuring incident angle and polarization on a commercial silicon photonic platform. This validates the first step in creating Shack-Hartmann-like wavefront sensors on chip for applications including atmospheric turbulence mitigation in FSO links. A single silicon photonic chip solution could serve as an alternative to AO systems and has advantages in speed, complexity, cost, and power consumption. These devices may lead to more reliable FSO satellite to ground links, providing connectivity to remote and rural areas in Canada.

References

[1] H. Kaushal and G. Kaddoum, "Free space optical communication: challenges and mitigation techniques," *ArXiv Prepr. ArXiv150604836*, 2015.

[2] "Introduction to the Electromagnetic Spectrum | Science Mission Directorate." https://science.nasa.gov/ems/01_intro (accessed Jul. 04, 2023).

[3] "Frequency bands used in satellite network | satellite frequency bands." https://www.rfwireless-world.com/Tutorials/satellite-frequency-bands.html (accessed Jul. 04, 2023).

[4] K. Rikkinen, P. Kyösti, M. E. Leinonen, M. Berg, and A. Pärssinen, "THz Radio Communication: Link Budget Analysis Towards 6G".

[5] K. Tekbıyık, A. Ekti, G. Karabulut Kurt, and A. Görçin, "Terahertz band communication systems: Challenges, novelties and standardization efforts," *Phys. Commun.*, vol. 35, May 2019, doi: 10.1016/j.phycom.2019.04.014.

[6] G. Rademacher *et al.*, "1.53 Peta-bit/s C-Band Transmission in a 55-Mode Fiber," in *2022 European Conference on Optical Communication (ECOC)*, Sep. 2022, pp. 1–4.

[7] S. Seel *et al.*, "Space to Ground bidirectional optical communication link at 5.6 Gbps and EDRS connectivity outlook," in *2011 Aerospace Conference*, Mar. 2011, pp. 1–7. doi: 10.1109/AERO.2011.5747331.

[8] L. Mohon, "Laser Communications Relay Demonstration (LCRD)," *NASA*, Jul. 14, 2015. http://www.nasa.gov/mission_pages/tdm/lcrd/index.html (accessed May 18, 2023).

[9] D. J. Israel, S. K. Vithlani, and B. Edwards, "Latest changes to NASA's laser communications relay demonstration project," in *Free-Space Laser Communication and Atmospheric Propagation XXX*, H. Hemmati and D. M. Boroson, Eds., San Francisco, United States: SPIE, Feb. 2018, p. 25. doi: 10.1117/12.2285221.

[10] F. Tavares, "NASA, Partners Achieve Fastest Space-to-Ground Laser Comms Link," *NASA*, May 11, 2023. http://www.nasa.gov/feature/ames/tbird-milestone (accessed May 18, 2023).

[11] C. M. Schieler *et al.*, "On-orbit demonstration of 200-Gbps laser communication downlink from the TBIRD CubeSat," in *Free-Space Laser Communications XXXV*, H. Hemmati and B. S. Robinson, Eds., San Francisco, United States: SPIE, Mar. 2023, p. 1. doi: 10.1117/12.2651297.

[12] F. Roddier, Ed., *Adaptive optics in astronomy*. Cambridge, U.K. ; New York: Cambridge University Press, 1999.

[13] T. Cherubini and S. Businger, "Another Look at the Refractive Index Structure Function," *J. Appl. Meteorol. Climatol.*, vol. 52, no. 2, pp. 498–506, Feb. 2013, doi: 10.1175/JAMC-D-11-0263.1.

[14] T. Cherubini, R. Lyman, and S. Businger, "Forecasting seeing for the Maunakea observatories with machine learning," *Mon. Not. R. Astron. Soc.*, vol. 509, no. 1, pp. 232–245, Nov. 2021, doi: 10.1093/mnras/stab2916.

[15] V. W. S. Chan, "Free-Space Optical Communications," *J. Light. Technol.*, vol. 24, no. 12, pp. 4750–4762, Dec. 2006, doi: 10.1109/JLT.2006.885252.
[16] M. Chen, C. Liu, D. Rui, and H. Xian, "Performance verification of adaptive optics for satellite-to-ground coherent optical communications at large zenith angle," *Opt. Express*, vol. 26, no. 4, pp. 4230–4242, Feb. 2018, doi: 10.1364/OE.26.004230.
[17] S. A. Al-Gailani *et al.*, "A Survey of Free Space Optics (FSO) Communication Systems, Links, and Networks," *IEEE Access*, vol. 9, pp. 7353–7373, 2021, doi: 10.1109/ACCESS.2020.3048049.
[18] C. I. Kourogiorgas, A. D. Panagopoulos, and J. D. Kanellopoulos, "On the Earth-Space Site Diversity Modeling: A Novel Physical-Mathematical Outage Prediction Model," *IEEE Trans. Antennas Propag.*, vol. 60, no. 9, pp. 4391–4397, Sep. 2012, doi: 10.1109/TAP.2012.2207073.
[19] E. Canada, "Astronomy Sky Condition - Environment Canada," Apr. 16, 2013. https://weather.gc.ca/astro/seeing_e.html (accessed Aug. 21, 2023).
[20] P. Taghinia, V. A. Muruganandan, R. M. Clare, and S. J. Weddell, "A Wavefront Sensorless Tip/Tilt Removal method for Correcting Astronomical Images," in *2020 35th International Conference on Image and Vision Computing New Zealand (IVCNZ)*, Nov. 2020, pp. 1–6. doi: 10.1109/IVCNZ51579.2020.9290688.
[21] L. C. Roberts *et al.*, "Performance of the adaptive optics system for Laser Communications Relay Demonstration's Ground Station 1," *Appl. Opt.*, vol. 62, no. 23, p. G26, Aug. 2023, doi: 10.1364/AO.486752.
[22] T. Weyrauch, M. A. Vorontsov, J. Gowens, and T. G. Bifano, "Fiber coupling with adaptive optics for free-space optical communication," in *Free-Space Laser Communication and Laser Imaging*, International Society for Optics and Photonics, 2002, pp. 177–184.
[23] H. Jian, D. Ke, L. Chao, Z. Peng, J. Dagang, and Y. Zhoushi, "Effectiveness of adaptive optics system in satellite-to-ground coherent optical communication," *Opt. Express*, vol. 22, no. 13, pp. 16000–16007, Jun. 2014, doi: 10.1364/OE.22.016000.
[24] J. Primot, "Theoretical description of Shack–Hartmann wave-front sensor," *Opt. Commun.*, vol. 222, no. 1, pp. 81–92, Jul. 2003, doi: 10.1016/S0030-4018(03)01565-7.
[25] A. Burvall, E. Daly, S. R. Chamot, and C. Dainty, "Linearity of the pyramid wavefront sensor," *Opt. Express*, vol. 14, no. 25, pp. 11925–11934, Dec. 2006, doi: 10.1364/OE.14.011925.
[26] C. Plantet *et al.*, "Adaptive optics with an infrared pyramid wavefront sensor at Keck," *J. Astron. Telesc. Instrum. Syst.*, vol. 6, no. 03, Sep. 2020, doi: 10.1117/1.JATIS.6.3.039003.
[27] S. Esposito and A. Riccardi, "Pyramid Wavefront Sensor behavior in partial correction AdaptiveOptic systems," *Astron. Astrophys.*, vol. 369, no. 2, pp. L9–L12, Apr. 2001, doi: 10.1051/0004-6361:20010219.
[28] S. Yi, J. Xiang, M. Zhou, Z. Wu, L. Yang, and Z. Yu, "Angle-based wavefront sensing enabled by the near fields of flat optics," *Nat. Commun.*, vol. 12, no. 1, p. 6002, Oct. 2021, doi: 10.1038/s41467-021-26169-z.

[29] K. M. Hampson, J. Antonello, R. Lane, and M. Booth, "Sensorless Adaptive Optics," Oct. 2020, doi: 10.5281/ZENODO.4065529.
[30] "Roadmap%20-%20Accepted%20version.doc."
[31] A. Mekis *et al.*, "A Grating-Coupler-Enabled CMOS Photonics Platform," *IEEE J. Sel. Top. Quantum Electron.*, vol. 17, no. 3, pp. 597–608, May 2011, doi: 10.1109/JSTQE.2010.2086049.
[32] S. Y. Siew *et al.*, "Review of Silicon Photonics Technology and Platform Development," *J. Light. Technol.*, vol. 39, no. 13, pp. 4374–4389, Jul. 2021, doi: 10.1109/JLT.2021.3066203.
[33] R. Baets *et al.*, "Silicon Photonics: silicon nitride versus silicon-on-insulator," in *Optical Fiber Communication Conference*, Anaheim, California: OSA, 2016, p. Th3J.1. doi: 10.1364/OFC.2016.Th3J.1.
[34] A. Rahim *et al.*, "Expanding the Silicon Photonics Portfolio With Silicon Nitride Photonic Integrated Circuits," *J. Light. Technol.*, vol. 35, no. 4, pp. 639–649, Feb. 2017, doi: 10.1109/JLT.2016.2617624.
[35] S. Liu *et al.*, "Thermo-optic phase shifters based on silicon-on-insulator platform: state-of-the-art and a review," *Front. Optoelectron.*, vol. 15, no. 1, p. 9, Dec. 2022, doi: 10.1007/s12200-022-00012-9.
[36] S. S. Azadeh *et al.*, "Low V_π Silicon photonics modulators with highly linear epitaxially grown phase shifters," *Opt. Express*, vol. 23, no. 18, p. 23526, Sep. 2015, doi: 10.1364/OE.23.023526.
[37] H. Sun, Q. Qiao, Q. Guan, and G. Zhou, "Silicon Photonic Phase Shifters and Their Applications: A Review," *Micromachines*, vol. 13, no. 9, p. 1509, Sep. 2022, doi: 10.3390/mi13091509.
[38] P. Edinger *et al.*, "Silicon photonic microelectromechanical phase shifters for scalable programmable photonics," *Opt. Lett.*, vol. 46, no. 22, pp. 5671–5674, Nov. 2021, doi: 10.1364/OL.436288.
[39] G. Chen *et al.*, "High-Speed Photodetectors on Silicon Photonics Platform for Optical Interconnect," *Laser Photonics Rev.*, vol. 16, no. 12, p. 2200117, 2022, doi: 10.1002/lpor.202200117.
[40] H. Li *et al.*, "Silicon Waveguide Integrated with Germanium Photodetector for a Photonic-Integrated FBG Interrogator," *Nanomaterials*, vol. 10, no. 9, p. 1683, Aug. 2020, doi: 10.3390/nano10091683.
[41] J. J. Ackert, A. S. Karar, D. J. Paez, P. E. Jessop, J. C. Cartledge, and A. P. Knights, "10 Gbps silicon waveguide-integrated infrared avalanche photodiode," *Opt. Express*, vol. 21, no. 17, pp. 19530–19537, Aug. 2013, doi: 10.1364/OE.21.019530.
[42] H. Mekawey, M. Elsayed, Y. Ismail, and M. A. Swillam, "Optical Interconnects Finally Seeing the Light in Silicon Photonics: Past the Hype," *Nanomaterials*, vol. 12, no. 3, p. 485, Jan. 2022, doi: 10.3390/nano12030485.
[43] C.-P. Hsu *et al.*, "A Review and Perspective on Optical Phased Array for Automotive LiDAR," *IEEE J. Sel. Top. Quantum Electron.*, vol. 27, no. 1, pp. 1–16, Jan. 2021, doi: 10.1109/JSTQE.2020.3022948.
[44] J. Notaros, M. Raval, M. Notaros, and M. R. Watts, "Integrated-Phased-Array-Based Visible-Light Near-Eye Holographic Projector," in *2019 Conference on Lasers*

and Electro-Optics (CLEO), May 2019, pp. 1–2. doi: 10.1364/CLEO_SI.2019.STu3O.4.

[45] C. V. Poulton *et al.*, "Long-range LiDAR and free-space data communication with high-performance optical phased arrays," *IEEE J. Sel. Top. Quantum Electron.*, vol. 25, no. 5, pp. 1–8, 2019.

[46] T. Watanabe, M. Ayata, U. Koch, Y. Fedoryshyn, and J. Leuthold, "Perpendicular Grating Coupler Based on a Blazed Antiback-Reflection Structure," *J. Light. Technol.*, vol. 35, no. 21, pp. 4663–4669, Nov. 2017, doi: 10.1109/JLT.2017.2755673.

[47] J. Notaros *et al.*, "Ultra-efficient CMOS fiber-to-chip grating couplers," in *2016 Optical Fiber Communications Conference and Exhibition (OFC)*, Mar. 2016, pp. 1–3.

[48] X. Chen, C. Li, C. K. Y. Fung, S. M. G. Lo, and H. K. Tsang, "Apodized Waveguide Grating Couplers for Efficient Coupling to Optical Fibers," *IEEE Photonics Technol. Lett.*, vol. 22, no. 15, pp. 1156–1158, Aug. 2010, doi: 10.1109/LPT.2010.2051220.

[49] Z. Zhao and S. Fan, "Design principles of apodized grating couplers," *J. Light. Technol.*, vol. 38, no. 16, pp. 4435–4446, Aug. 2020, doi: 10.1109/JLT.2020.2992574.

[50] F. Van Laere *et al.*, "Compact and Highly Efficient Grating Couplers Between Optical Fiber and Nanophotonic Waveguides," *J. Light. Technol.*, vol. 25, no. 1, pp. 151–156, Jan. 2007, doi: 10.1109/JLT.2006.888164.

[51] H. Zhang *et al.*, "Efficient silicon nitride grating coupler with distributed Bragg reflectors," *Opt. Express*, vol. 22, no. 18, p. 21800, Sep. 2014, doi: 10.1364/OE.22.021800.

[52] J. Wang, I. Glesk, and L. R. Chen, "Subwavelength grating devices in silicon photonics," *Sci. Bull.*, vol. 61, no. 11, pp. 879–888, Jun. 2016, doi: 10.1007/s11434-016-1077-z.

[53] L. Cheng, S. Mao, Y. Wang, and H. Y. Fu, "Fiber-Chip Bi-Wavelength Multiplexing With Subwavelength Single-Etch Grating Coupler and Diplexer," *IEEE Photonics J.*, vol. 14, no. 1, pp. 1–6, Feb. 2022, doi: 10.1109/JPHOT.2022.3143689.

[54] Y. Ding, C. Peucheret, H. Ou, and K. Yvind, "Fully etched apodized grating coupler on the SOI platform with −058 dB coupling efficiency," *Opt. Lett.*, vol. 39, no. 18, p. 5348, Sep. 2014, doi: 10.1364/OL.39.005348.

[55] D. Taillaert, Harold Chong, P. I. Borel, L. H. Frandsen, R. M. De La Rue, and R. Baets, "A compact two-dimensional grating coupler used as a polarization splitter," *IEEE Photonics Technol. Lett.*, vol. 15, no. 9, pp. 1249–1251, 2003, doi: 10.1109/LPT.2003.816671.

[56] W. Bogaerts, D. Taillaert, P. Dumon, D. Van Thourhout, R. Baets, and E. Pluk, "A polarization-diversity wavelength duplexer circuit in silicon-on-insulator photonic wires," *Opt. Express*, vol. 15, no. 4, p. 1567, Feb. 2007, doi: 10.1364/OE.15.001567.

[57] Y. Wei, H. Zhou, J. Dong, and X. Zhang, "On-chip Stokes Polarimeter Based on a Two-dimensional Grating," in *2019 Photonics & Electromagnetics Research*

Symposium - Fall (PIERS - Fall), Dec. 2019, pp. 1185–1190. doi: 10.1109/PIERS-Fall48861.2019.9021695.

[58] F. Van Laere *et al.*, "Compact Focusing Grating Couplers for Silicon-on-Insulator Integrated Circuits," *IEEE Photonics Technol. Lett.*, vol. 19, no. 23, pp. 1919–1921, Dec. 2007, doi: 10.1109/LPT.2007.908762.

[59] F. Van Laere, W. Bogaerts, P. Dumon, Gü. Roelkens, D. Van Thourhout, and R. Baets, "Focusing Polarization Diversity Grating Couplers in Silicon-on-Insulator," *J. Light. Technol.*, vol. 27, no. 5, pp. 612–618, Mar. 2009, doi: 10.1109/JLT.2008.2004946.

[60] A. Håkansson and J. Sánchez-Dehesa, "Inverse designed photonic crystal de-multiplex waveguide coupler," *Opt. Express*, vol. 13, no. 14, p. 5440, Jul. 2005, doi: 10.1364/OPEX.13.005440.

[61] J. Covey and R. T. Chen, "Efficient perfectly vertical fiber-to-chip grating coupler for silicon horizontal multiple slot waveguides," *Opt. Express*, vol. 21, no. 9, pp. 10886–10896, May 2013, doi: 10.1364/OE.21.010886.

[62] Y. Zhang *et al.*, "A compact and low loss Y-junction for submicron silicon waveguide," *Opt. Express*, vol. 21, no. 1, p. 1310, Jan. 2013, doi: 10.1364/OE.21.001310.

[63] A. M. Hammond, J. B. Slaby, M. J. Probst, and S. E. Ralph, "Multi-layer inverse design of vertical grating couplers for high-density, commercial foundry interconnects," *Opt. Express*, vol. 30, no. 17, pp. 31058–31072, Aug. 2022, doi: 10.1364/OE.466015.

[64] N. V. Sapra *et al.*, "Inverse Design and Demonstration of Broadband Grating Couplers," *IEEE J. Sel. Top. Quantum Electron.*, vol. 25, no. 3, pp. 1–7, May 2019, doi: 10.1109/JSTQE.2019.2891402.

[65] A. Michaels and E. Yablonovitch, "Inverse design of near unity efficiency perfectly vertical grating couplers," *Opt. Express*, vol. 26, no. 4, pp. 4766–4779, Feb. 2018, doi: 10.1364/OE.26.004766.

[66] W.-K. Chen, Ed., *The electrical engineering handbook*. Amsterdam ; Boston: Elsevier Academic Press, 2005.

[67] "Maxwell's Equations." https://maxwells-equations.com/ (accessed Jan. 19, 2023).

[68] "OptiFDTD_Technical_Background.pdf."

[69] C. M. Lalau-Keraly, S. Bhargava, O. D. Miller, and E. Yablonovitch, "Adjoint shape optimization applied to electromagnetic design," *Opt. Express*, vol. 21, no. 18, pp. 21693–21701, Sep. 2013, doi: 10.1364/OE.21.021693.

[70] A. F. Oskooi, D. Roundy, M. Ibanescu, P. Bermel, J. D. Joannopoulos, and S. G. Johnson, "Meep: A flexible free-software package for electromagnetic simulations by the FDTD method," *Comput. Phys. Commun.*, vol. 181, no. 3, pp. 687–702, Mar. 2010, doi: 10.1016/j.cpc.2009.11.008.

[71] "NanoSOI Fabrication Service | Applied Nanotools Inc.," Mar. 26, 2020. https://www.appliednt.com/nanosoi-fabrication-service/ (accessed Feb. 15, 2022).

[72] L. Chrostowski and M. Hochberg, *Silicon Photonics Design*. Cambridge: Cambridge University Press, 2015. doi: 10.1017/CBO9781316084168.

[73] A. Yariv, P. Yeh, and A. Yariv, *Photonics: optical electronics in modern communications*, 6th ed. in The Oxford series in electrical and computer engineering. New York: Oxford University Press, 2007.
[74] *Topic 7b -- Slab waveguide analysis*, (Feb. 26, 2018). Accessed: Jul. 05, 2023. [Online Video]. Available: https://www.youtube.com/watch?v=Sh0XjszSjVw
[75] "OptiFDTD," *Optiwave*. https://optiwave.com/products/optifdtd/ (accessed Sep. 01, 2023).
[76] A. Milton and W. Burns, "Mode coupling in optical waveguide horns," *IEEE J. Quantum Electron.*, vol. 13, no. 10, pp. 828–835, Oct. 1977, doi: 10.1109/JQE.1977.1069240.
[77] Y. Fu, T. Ye, W. Tang, and T. Chu, "Efficient adiabatic silicon-on-insulator waveguide taper," *Photonics Res.*, vol. 2, no. 3, pp. A41–A44, Jun. 2014, doi: 10.1364/PRJ.2.000A41.
[78] "KLayout Layout Viewer And Editor." https://www.klayout.de/ (accessed Sep. 01, 2023).
[79] "Gdspy's Documentation — gdspy 1.6.13 documentation." https://gdspy.readthedocs.io/en/stable/ (accessed Sep. 01, 2023).
[80] "Image Processing Toolbox." https://www.mathworks.com/products/image.html (accessed Sep. 01, 2023).
[81] X. Chen and H. K. Tsang, "Nanoholes Grating Couplers for Coupling Between Silicon-on-Insulator Waveguides and Optical Fibers," *IEEE Photonics J.*, vol. 1, no. 3, pp. 184–190, Sep. 2009, doi: 10.1109/JPHOT.2009.2031685.
[82] S. Lischke *et al.*, "Ultra-fast germanium photodiode with 3-dB bandwidth of 265 GHz," *Nat. Photonics*, vol. 15, no. 12, Art. no. 12, Dec. 2021, doi: 10.1038/s41566-021-00893-w.
[83] V. Akondi and A. Dubra, "Shack-Hartmann wavefront sensor optical dynamic range," *Opt. Express*, vol. 29, no. 6, p. 8417, Mar. 2021, doi: 10.1364/OE.419311.
[84] B. R. M. Norris, J. Wei, C. H. Betters, A. Wong, and S. G. Leon-Saval, "An all-photonic focal-plane wavefront sensor," *Nat. Commun.*, vol. 11, no. 1, p. 5335, Oct. 2020, doi: 10.1038/s41467-020-19117-w.
[85] S. Janz *et al.*, "Si-Photonic Waveguide Grating Coupler Arrays for Wavefront Monitoring," in *2022 Photonics North (PN)*, May 2022, pp. 1–1. doi: 10.1109/PN56061.2022.9908321.
[86] G. S. Jayabalan and J. F. Bille, "The Development of Adaptive Optics and Its Application in Ophthalmology," in *High Resolution Imaging in Microscopy and Ophthalmology: New Frontiers in Biomedical Optics*, J. F. Bille, Ed., Cham: Springer International Publishing, 2019, pp. 339–358. doi: 10.1007/978-3-030-16638-0_16.
[87] E. Akyol, A. M. Hagag, S. Sivaprasad, and A. J. Lotery, "Adaptive optics: principles and applications in ophthalmology," *Eye*, vol. 35, no. 1, Art. no. 1, Jan. 2021, doi: 10.1038/s41433-020-01286-z.
[88] E. Brunner *et al.*, "Retinal adaptive optics imaging with a pyramid wavefront sensor," *Biomed. Opt. Express*, vol. 12, no. 10, pp. 5969–5990, Oct. 2021, doi: 10.1364/BOE.438915.

[89] Z. Zhou *et al.*, “Adaptive optical microscopy via virtual-imaging-assisted wavefront sensing for high-resolution tissue imaging,” *PhotoniX*, vol. 3, no. 1, p. 13, May 2022, doi: 10.1186/s43074-022-00060-6.

[90] S. Hu, L. Hu, W. Gong, Z. Li, and K. Si, “Deep learning based wavefront sensor for complex wavefront detection in adaptive optical microscopes,” *Front. Inf. Technol. Electron. Eng.*, vol. 22, no. 10, pp. 1277–1288, 2021.